BAB

library

MET O 11 TECHNICAL NOTE NO. 165
(Incorporates Technical Note No. 158)

SIMULATION OF ATMOSPHERIC HYDRAULIC JUMPS IN THE PRESENCE OF ROTATION AND MOUNTAINS

C A Parrett and M J P Cullen

Met O 11 (Forecasting Research Branch),
Meteorological Office,
London Road,
Bracknell,
Berkshire,
RG12 2SZ,
England

February 1983

N.B. This paper has not been published. Permission to quote from it must be obtained from the Assistant Director of the above Meteorological Office Branch.

Summary

Numerical solutions of the shallow water equations in one-dimension are presented. The formation and evolution of hydraulic jumps is predicted with a simple centred finite difference model and with a model utilising Glimm's method. Glimm's method is a special one-dimensional method, which has been proved to converge to the physically relevant solution of a number of equations in the presence of discontinuities. The solution from it is used to check the finite difference method.

Cases presented include examples of jumps produced in the presence of rotation, and a variety of jumps forced by flow over orography. It is shown that a conservative finite difference method, with the addition of artificial diffusion, converges to the correct solution for almost all cases. However, the use of multipoint filters gives poor results. At low resolution, the errors in modelling the flow induced by the orography are larger than errors caused by not resolving the shape of the orography.

1. Introduction

A mid-latitude front is probably the best-known example of a near-discontinuity in the atmosphere (at which the temperature, wind velocity and pressure gradient tend to be discontinuous); diffusion and turbulent mixing generated by the large wind shear prevent the formation of an actual discontinuity. Most numerical models of the atmosphere use finite difference methods, and these can produce oscillations or blow up near discontinuities due to their inherent assumption of regularity of the solution. Consequently, some form of artificial diffusion or filtering is incorporated in order to eliminate these oscillations. But, from other branches of computational fluid dynamics it is known that using such measures does not necessarily produce convergence to the correct physical solution. Therefore, in trying to model the formation and evolution of discontinuities in the atmosphere, models may generate spurious solutions, which would lead to errors in the forecasts. This is more likely to be a problem in fine-mesh and meso-scale

models, which can resolve the discontinuities better than the large-scale coarse-mesh models. It may however become more relevant to large-scale models as forecasts are extended in time.

As a first step towards investigating the representation of discontinuities in numerical models, we use two different methods to look at the formation and evolution of hydraulic jumps in a one-dimensional, homogeneous, inviscid, one-layer fluid; including rotation and bottom topography in the model. We therefore solve the one-dimensional shallow water equations

$$\begin{aligned} \frac{\partial u}{\partial t} + u\frac{\partial u}{\partial x} + \frac{\partial \phi}{\partial x} &= fv - g\frac{\partial H}{\partial x} \\ \frac{\partial v}{\partial t} + u\frac{\partial v}{\partial x} &= -fu \\ \frac{\partial \phi}{\partial t} + u\frac{\partial \phi}{\partial x} + \phi\frac{\partial u}{\partial x} &= 0 \end{aligned} \qquad (1)$$

where $\phi = gh$, h = depth of fluid, f = Coriolis parameter, H = height of bottom topography, and all variables are assumed independent of y. This model may have direct application to various meso-scale phenomena in the atmosphere, which it is claimed are analogous to hydraulic jumps (eg squall lines (Tepper 1950), and some mountain winds (Houghton and Kasahara 1968)).

The two methods that we use are an ordinary finite difference method using centred time and space differencing and with the equations written in flux form (the FDM), and an extension of Glimm's method (GM) (Glimm 1965, Lax 1973) with which to compare the FDM. Glimm's method can be rigorously proved to converge to the correct physical solution of certain systems of equations similar to (1). More generally, if it is found to converge in practice to a bounded solution of such equations then that solution will be the physically correct one. It is therefore a useful method for checking that finite difference models are converging to the right answer. However, its practical use for atmospheric models is limited, since these theoretical advantages only apply in one dimension. The best that can be hoped for is that if a finite difference method can be demonstrated to give the

correct solution in one dimension it will continue to do so in higher dimensions. There is no way of proving this at present.

GM and the FDM are described in sections 2 and 3, respectively, followed by an account of the numerical experiments in section 4 and a discussion in section 5.

2. Glimm's Method

The solution in Glimm's method is constructed by representing the initial data as piece-wise constant, solving the equations exactly over one time-step, and then constructing a new piece-wise constant field by a sampling procedure. The advantage of GM is that it can track discontinuities without requiring any artificial viscosity. The method is only summarised here, details are given in the Appendix.

The method evolved from Glimm's constructive existence proof for solving non-linear hyperbolic systems of conservation laws (Glimm 1965, Lax 1973), and was developed by Chorin (1976) as a numerical method. Recently it has been used to solve the one-dimensional shallow water equations without any orography or rotation (Marshall and Mendez 1981, henceforth referred to as MM). Here we have followed a similar procedure to that detailed in MM, but have extended the method to include rotation and bottom topography, so as to be able to solve the system of equations (1).

Glimm's method constructs the solution forward in time by means of two identical fractional steps. To illustrate the first step and define the method, we consider a single conservation law,

$$\frac{\partial u}{\partial t} + \frac{\partial}{\partial x} f(u) = 0 \qquad (2) .$$

Let Δx and Δt be the space and time increments, i and n be integers, and let $u_i^n \equiv u(i\Delta x, n\Delta t)$. At time $t_n = n\Delta t$ the method approximates the solution u with piece-wise constant data $u(x,t_n) = u_i^n \quad , \quad x < (i+\tfrac{1}{2})\Delta x$

$= u_{i+1}^n \quad , \quad x \geqslant (i+\tfrac{1}{2})\Delta x$

(where $i\Delta x \leqslant x \leqslant (i+1)\Delta x$). This defines a succession of Riemann

problems (one for each intermediate point $(i+\frac{1}{2})\Delta x$), which are to be solved exactly to give the solutions at time $(n+\frac{1}{2})\Delta t$, $u'(x, t_{n+\frac{1}{2}})$. These new solutions are then each sampled to obtain the values for the intermediate points. The position of the sampling point P_i for each interval $[i\Delta x, (i+1)\Delta x]$ is given by $P_i = (i+\theta_i)\Delta x$, where θ_i is the value of a pseudo-random variable θ, equidistributed in $[0,1]$. $u'(P_i, t_{n+\frac{1}{2}})$ is the value of the solution of the Riemann problem at P_i, and this is the value which is assigned to u at the point $(i+\frac{1}{2})\Delta x$ at time $(n+\frac{1}{2})\Delta t$, ie $u_{i+\frac{1}{2}}^{n+\frac{1}{2}} = u'(P_i, t_{n+\frac{1}{2}})$. Thus the solution is advanced by half a time-step to $t_{n+\frac{1}{2}}$. The second step advances the solution from $t_{n+\frac{1}{2}}$ to t_{n+1} in a similar manner, to give the values of u at the grid-points ready to begin the next time-step.

Given the solution to the Riemann problem, its behaviour is largely determined by the values of θ_i (ie the sampling positions P_i). It is important that the θ_i tend as fast as possible to equidistribution on $[0,1]$. The strategy of selecting a new value of θ for each grid-point has been shown to be disastrous, because of the generation of spurious constant states (Chorin 1976). Consequently we adopted the policy of choosing a new θ for each (half) time-step only, utilising a (p_1, p_2) van der Corput sequence. This is an equidistributed sequence defined by $b^k = \sum_{l=0}^{m} q_l p_1^{-(l+1)}$, where $q_l = p_2 i_l \bmod p_1$, $\sum_{l=0}^{m} i_l p_1 = k$, and p_1, p_2 are integers, $p_1 > p_2 > 0$ (Colella 1982). For our experiments we used either a binary $(p_1 = 2, p_2 = 1)$, or a (3, 2), or a (5, 3) van der Corput sequence, after finding that they compared favourably with other van der Corput sequences. In most previous work using GM, random sampling has been used (together with a variance reduction technique); we also tried using such sequencies of pseudo-random numbers as in Chorin (1976), but found that the van der Corput sequences gave more consistent and smoother results for the same resolution.

Glimm's method cannot be used to solve the inhomogeneous equations (1) as they stand, so a splitting technique was used. Firstly consider the homogeneous part of equations (1):

$$\frac{\partial}{\partial t}(\phi u) + \frac{\partial}{\partial x}(\phi u^2 + \tfrac{1}{2}\phi^2) = 0 \qquad (3)$$

$$\frac{\partial}{\partial t}(\phi v) + \frac{\partial}{\partial x}(\phi u v) = 0 \qquad (4)$$

$$\frac{\partial}{\partial t}\phi + \frac{\partial}{\partial x}(\phi u) = 0 \qquad (5)$$

These can be solved directly using GM and the analogy with gas dynamics utilised in MM (see Appendix for details). It is found from the jump conditions derived from system (3), (4), (5) that v is continuous across a jump in ϕ and u; but it may be discontinuous across a slip line, where u is continuous. Equation (4) is uncoupled from (3) and (5), and since it does not interact with the jump conditions for ϕ and u it can be solved separately in the form

$$\frac{\partial v}{\partial t} + u\frac{\partial v}{\partial x} = 0 \qquad (6)$$

If (6) is solved assuming a piece-wise constant v profile, spurious constant states are introduced into the solution. We therefore assumed an initial piece-wise linear v profile between grid-points. Then, to obtain $v_{i+\frac{1}{2}}^{n+\frac{1}{2}}$, the appropriate value of $v^n(x)$ was advected with the new x-component of velocity at $(i+\frac{1}{2})\Delta x$, $(n+\frac{1}{2})\Delta t$ (Fig. 1).

These estimates of $u_{i+\frac{1}{2}}^{n+\frac{1}{2}}$ and $v_{i+\frac{1}{2}}^{n+\frac{1}{2}}$ ($\hat{u}$ and $\hat{v}$, say), from equations (3) to (6), were then updated with the Coriolis terms. This was achieved by a rotation of the velocity vector $\underline{\hat{u}} = (\hat{u}, \hat{v})$ through an angle $f\Delta t/2$ (for each fractional $\frac{1}{2}$ time-step). Secondly, the orographic term was added to $u((i+\frac{1}{2})\Delta x)$ in the centred finite difference form $g(H_{i+1} - H_i)\Delta t/2\Delta x$. An alternative method of incorporating this term (and also a friction term) into GM without splitting has been reported by Marshall and Menendez (1981) for a constant sloping bottom topography. This method proved unsuccessful for our more complex bottom topography.

Glimm's method is essentially a one-dimensional technique and it is not applicable to multidimensional atmospheric models. In any case it is much more expensive on computer time, and for our model GM took about 20 times more CPU time than the FDM. GM has been used in two dimensions with a form of operator splitting, but was found to introduce large errors unless used in conjunction with another method as a hybrid scheme (Colella 1982).

3. The finite difference scheme

For the finite difference method (FDM), equations (1) were written in flux form and diffusion terms were added, to give the following system of equations:

$$\begin{aligned}
\frac{\partial}{\partial t}(\phi u) + \frac{\partial}{\partial x}(\phi u^2 + \tfrac{1}{2}\phi^2) &= f\phi v - g\frac{\partial H}{\partial x} + K\frac{\partial^2}{\partial x^2}(\phi u) \\
\frac{\partial}{\partial t}(\phi v) + \frac{\partial}{\partial x}(\phi u v) &= -f\phi u + K\frac{\partial^2}{\partial x^2}(\phi v) \\
\frac{\partial}{\partial t}\phi + \frac{\partial}{\partial x}(\phi u) &= K\frac{\partial^2}{\partial x^2}\phi
\end{aligned} \qquad (7)$$

(K = diffusion coefficient). These equations were then solved numerically by discreting them into the following form (where $m = \phi u$ and $n = \phi v$):

$$\begin{aligned}
m_i^{n+1} &= m_i^{n-1} - 2\Delta t\Big\{\big[(u_{i+1}^n + u_i^n)(m_{i+1}^n + m_i^n) - (u_i^n + u_{i-1}^n)(m_i^n + m_{i-1}^n) + \phi_{i+1}^{n^2} - \phi_{i-1}^{n^2}\big]/4\Delta x \\
&\qquad - f n_i^n - K(m_{i+1}^{n-1} - 2m_i^{n-1} + m_{i-1}^{n-1})/\Delta x^2\Big\} \\
n_i^{n+1} &= n_i^{n-1} - 2\Delta t\Big\{\big[(v_{i+1}^n + v_i^n)(m_{i+1}^n + m_i^n) - (v_i^n + v_{i-1}^n)(m_i^n + m_{i-1}^n)\big]/4\Delta x \\
&\qquad + f m_i^n - K(n_{i+1}^{n-1} - 2n_i^{n-1} + n_{i-1}^{n-1})/\Delta x^2\Big\} \qquad (8) \\
\phi_i^{n+1} &= \phi_i^{n-1} - 2\Delta t\big\{(m_{i+1}^n - m_{i-1}^n)/2\Delta x - K(\phi_{i+1}^{n-1} - 2\phi_i^{n-1} + \phi_{i+1}^{n-1})/\Delta x^2\big\} ,
\end{aligned}$$

where centred time differencing has been used, except for the diffusion terms, which were forward-differenced in order to ensure stability. Forward time differences were used for the first time-step for all terms.

4. Numerical experiments

a. Experiments without topography

The initial fields for the first set of experiments were given by

$$u(x,0) = U\cos(x/L)$$

$$v(x,0) = 0 \qquad (9)$$

$$\phi(x,0) = \phi_m + U\{(U/8)\cos(2x/L) + (\phi_m - U^2/8)^{1/2}\cos(x/L)\}$$

where the length of the domain = $2\pi L$, $\phi_m = g h_m$, h_m = mean height of the fluid, and U = constant. These are the same as those used by Williams and Hori (1970) (henceforth referred to as WH) and are shown in Fig. 2. Following WH, the results presented here are in the form of profiles of the non-dimensional variables $u' = u/U$, $v' = v/U$ and $h' = (\phi - \phi_m)/U\phi_m^{1/2}$, and the time t is given in units of the advective time scale L/U. Periodic boundary conditions were enforced; and $\Delta x = 2\pi L/N$, where $N = 320$ for the results presented.

The formation of hydraulic jumps in the presence of rotation was shown by WH to depend on two non-dimensional parameters, the Rossby number $R_o = U/fL$ and the Froude number $F = U/\phi_m^{1/2}$. Here we repeat and extend WH's results for a case with F = 1.0 and Ro= 1.0, in which a jump forms. They showed that for a higher rotation rate (Ro = 0.1) jump formation was prevented, or at least severely delayed, with just an inertial oscillation in the wind velocity. With Ro = 1.0 the rotation was no longer dominant and was unable to prevent the formation of a jump. This formation and subsequent evolution of the jump, as modelled by GM (using a (5,3) van der Corput sampling sequence), is shown in Figs 2-6. One can immediately see that GM produces rather rough profiles; this is due to the pseudo-random sampling and to the fact that the method is only first-order accurate. Once the jump has formed, by $t = 0.7\,L/U$ (Fig. 3), one can see that it

then sharpens and travels forward, while a trough forms in h behind the jump, resulting in a sharp 'spike' in the h profile at the jump by $t = 1.4\,L/U$ (Fig. 4). The v profile remains continuous but develops a sharp discontinuity in slope at the jump. As the spike in h moves forward up the slope ahead of the jump, the jump in u, which had reached a maximum near $t = 1.4\,L/U$, can be seen to decrease somewhat (Figs 4 and 5). At the same time a more marked minimum in v has developed behind the jump due to the action of the Coriolis force on the earlier high values of u behind the jump. By $t = 2.8\,L/U$ (Fig. 6) what had earlier been a sharp maximum in v at the jump has broadened due to the interaction of the jump with a smooth wave travelling in the opposite direction. The jump itself propagates forwards with no dissipation, as expected with GM.

Figure 7 shows the results at $t = 2.8\,L/U$ for an equivalent run of the experiment with the FDM (using the same number of grid-pints, and with $K = 2.5 \times 10^4\ m^2 s^{-1}$). The profiles are similar to those produced by GM, as they are for earlier times (not shown). The u and h profiles are much smoother, and the jump has been smeared over 4 or 5 grid-lengths due to the artificial diffusion present in the FDM. Thus the sharp spike in h, present in the results using GM, has been smoothed out, with a consequent loss of about 5% in the amplitude of the jump in h.

Superimposed on Fig. 7 is the h profile resulting from the use of a finite difference method using a non-conservative formulation of the equations (system (1) was solved with the equations as they stand, using centred differences and diffusing u, v and ϕ). It illustrates the errors introduced by using such a scheme when the solution can become discontinuous. The jump is seen to be in the wrong position and its amplitude is too small. Both errors seem to have originated soon after jump formation, when the jump moved much slower, and this was associated

with lower values of u behind the jump. The adverse effects of using a non-conservative scheme are well known in gas dynamics.

Multipoint filters are sometimes used in numerical models, either in place of diffusion or in combination with it (e.g. Francis 1975); and, as a comparison, we carried out several repeat runs of the above FDM experiment using filters instead of diffusion. We used linear filters, Shapiro (1971), of order 2, 4 and 8, applied to m, n and ϕ at each time-step. The 5-point filter gave results very close to those with artificial diffusion, which is effectively a first-order filter, but a few (small amplitude) oscillations developed near the jump soon after it formed; although these were contained near the jump and did not grow with time. Similar results were obtained with the 9-point filter; and, although the amplitude of the oscillations was somewhat larger and they had a shorter wavelength, as the resolution was increased the solution could be seen to converge to the correct one, except for a small positive error in the jump speed. With the 17-point filter the oscillations were much larger, had a shorter wavelength and were more extensive; although the correct solution is still just recognizable at $t = 1.05\, L/u$ (Fig. 8), soon after jump formation. By $t = 2.8\, L/u$ (Fig. 9) the solution can be seen to have deteriorated badly, with wave packets propagating away from the jump region, the oscillation peaks have become spiked and the troughs flattened, and the jump is being dissipated. Though the 8th order filter completely damps two and three grid-length waves, it leave waves longer than four grid-lengths completely undamped and is thus unable to capture the jump. This is because the Fourier analysis of a jump comprises a whole spectrum of wavelengths; those of $4\Delta x$ or longer will not be removed by the filter, and will thus corrupt the solution. The lower order filters are less scale-selective and produce more damping of the longer waves as well as of the very short waves. Therefore, for modelling of discontinuities, the use of low-

order filters (or diffusion) is preferred to the use of high order filters.

b. Experiments including bottom topography

These experiments continue the work of Houghton and Kasahara (1968) (henceforth denoted by HK). They looked at the criteria for jump formation over an isolated ridge, without rotation, both analytically and numerically. They found three classes of motion dependent on the initial Froude number F and the ridge height H_c : subcritical and supercritical motion without jumps, and for intermediate flow speeds a flow regime in which jumps formed on both sides of the ridge. We have concentrated on one case that HK presented (their case C) when jumps formed. In this case one jump moved upstream from the ridge and another moved slowly downstream. We present results for their problem, and then further experiments in which rotation is added and a perturbation is propagated over the ridge. For these three experiments results are shown comparing the FDM with GM. Lastly, we present results of an experiment on the importance of the representation of the shape of topography within the FDM.

The initial conditions for the experiments were the same as those given in HK: $h_0 = 20\,cm$, $\Delta x = 1.0\,cm$, length of domain $L = N\Delta x$ ($N = 2000$ for most experiments), $u_0 = 0.98\,ms^{-1}$, $v_0 = 0$, $F = 0.7$ and $\Delta t = 0.82\,\Delta x / (u_0 + (g h_0)^{1/2})$. At $t = 0$ the fluid was impulsively set into motion with constant velocity u_0 from a state of rest with a flat upper surface at height h_0. Except for the final experiment the ridge had a smooth convex shape in cross-section, given by $H(x) = H_c(1 - x^2/a^2)$ for $0 \leq |x| \leq a$, where $H_c = 0.5\,h_0$, $a = 0.4\,m$ and the origin was at the centre of the domain. The domain was periodic in x, with the boundaries set far enough from the ridge so that transient waves stimulated by the impulsive start were not fed back in to affect the 'steady-state' solution.

The diffusion coefficient in the FDM was $K = 2 \times 10^{-3}\ m^2 s^{-1}$, except in the final low resolution experiments. The results are presented as profiles of the non-dimensional variables $u' = Fu/u_o$, $v' = Fv/u_o$ and $h' = h/h_o$.

(i) Repeat of HK's experiment

The results after 400 time-steps are shown in Figs. 10 and 11 (corresponding to Fig. 14c in HK), where a (3, 2) van der Corput sampling sequence was used in GM (Fig. 11). The results using the FDM (Fig. 10) are in good agreement with HK's results from a Lax Wendroff finite difference model. Comparing the results with those from GM, there are only minor differences in the profiles, with the expected roughnesses produced by GM in the 'smooth' regions. The FDM produced some smearing of the jumps, and also produced a few oscillations behind the downstream-moving jump. The roughnesses seen in the profiles of Fig. 11 upstream of the ridge were caused by the sampling sequence used in GM, with different sequences producing different patterns; the mean of several different runs agreed with a higher resolution solution. The FDM therefore seems to have given the correct answer for this case. A similar experiment was carried out where the smooth convex ridge was replaced by a rectangular shaped one. The FDM again gave the same solution as GM, although both sets of profiles were much rougher near the edges of the ridge.

(ii) Inclusion of rotation:

The experiment described above was repeated several times with the addition of rotation. The initial Rossby number, $R_o = u_o / fD$, was first set equal to 0.1 (where the length scale D was taken as the width of the ridge). For this high rotation rate case (as in section (a)) jumps were prevented from forming within the integration period ($O(f^{-1})$) and we simply obtained an inertial oscillation in the wind field with small amplitude smooth waves propagating away from the ridge. As expected, the FDM gave the correct answer for this continuous solution, giving almost identical results to those obtained with GM.

Figures 12 and 13 show results obtained with Ro = 1.0. (Note that a larger section of the domain is shown here compared to that in Figs. 10 and 11, and consequently a transient wave set up by the impulsive start is visible towards the right of the diagrams). As for the flat-bottom case presented in (a), the rotation rate here was not high enough to prevent the formation of jumps; but it has made the profiles more complex by reversing the flow over the ridge by the time shown, so that the original downstream jump had become an upstream one, which had propagated back over the ridge. Despite the complexity, the results from the FDM are seen to compare very well with those from GM (in which a binary van der Corput sampling sequence was used). As previously, the only errors in the FDM are a slight smearing of the jumps and small oscillations behind the jumps, and these seem to have had no adverse effect on the overall solution.

(iii) Propagation of a perturbation over the ridge

The next stage was to see how the FDM handled the interaction as a transient wave propagated over the ridge and through the 'steady-state' system that had formed without rotation. To produce the transient, a sine-wave perturbation (hump), with maximum amplitude of $0.8h_o$, was added to the initial h profile well upstream of the ridge. This was then simply allowed to interact with the velocity field and split into two equal-sized waves propagating in different directions, so that one of these waves moved over the ridge as required, but not until the 'steady-state' had been established.

The forward edge of the transient wave reached the ridge at about $t = 1.4\,s$ (the time of the profiles shown in Figs. 10 and 11), at which time there was very good agreement between the FDM and GM. However, by $t = 2.1\,s$ there was some discrepancy between the two methods, which increased by $t = 2.4\,s$ (Fig. 14). The FDM produced lower values of both u and h over most of the emerging transient wave, but at the wave's leading edge, where a jump had formed, it produced slightly higher values. Thus, the FDM results give the impression that the peak of the wave moved too fast and produced a larger jump moving slightly too fast. The error in the jump amplitude was about 7%, and the maximum error behind the jump was about $2\frac{1}{2}$% of the absolute values. The effect remained much the same as the transient wave continued to move away from the ridge.

(iv) Experiments on the representation of topography in the FDM

The final results presented here used the same initial conditions as in (i), (ii) and (iii), but the orography consisted of two sine-squared shaped ridges next to each other. This double ridge was represented in the FDM in two different ways: each grid-point was assigned (I) the integrated mean value of H, and (II) the maximum value of H, over the grid-length surrounding it. These two representations were compared as the resolution in the model was decreased.

Generally, the differences between the high resolution solution (with 2000 grid-points) and both sets of low resolution results were much greater than the differences between the solutions from (I) and (II) themselves. The two representations gave qualitatively similar results, although there were quite large quantitive differences. Figures 15 and 16 show an example with a resolution of 50 points, with the high

resolution profiles of h and H added to both figures. From the high resolution profile of h one can see that the upstream and downstream jumps formed in a similar manner to the case with just one ridge; but there was another jump produced inbetween the ridges, and this moved slowly upstream. Although there is little to choose between (I) and (II) for the region between the ridges, either side of the ridges run (II) (with the maximum height of topography) produced larger jumps, with profiles closer to the correct ones; in particular, the upstream blocking effect was better represented, since the height of the ridges was correct in this case. Because of the greater width of the ridges in (II) their effect was spread further downstream. As the resolution was further decreased and the ridge height in (I) was reduced, the solution from this case was smoothed considerably compared to that in (II), with the blocking effect in particular being greatly reduced.

It is difficult to say whether these effects are important for full three-dimensional numerical models. Obviously in a more complete model there would be the added complications of elevated heat sources and the release of latent heat over mountains. These results do, nevertheless, illustrate some errors which might occur in the dynamics of airflow over mountains as represented in small-scale models, and lend some support to the idea (eg Wallace et al 1982) that the use of averaged topographic height over grid squares in models could be improved upon.

5. Discussion

This paper has compared the evolution of hydraulic jumps using finite difference methods against reference solutions obtained using Glimm's Method. The agreement was very close, provided that the mass and momentum were conserved. The results using a simple centred differencing scheme appear to have been quite adequate, with no need to resort to the many more complex schemes derived for use in shock modelling. In the presence of rotation there was a danger that spurious information could have been generated if the jump was not sharp; however this does not seem to have occurred. The only (small) discrepancies were in the experiment described in section (b) (iii), in which a transient wave propagated over the ridge. This may have been the most realistic case in meteorological terms, and may indicate that errors can be produced in meso-scale models when modelling small-scale features impinging on mountain ranges. The results from our final experiment indicate that smoothing of poorly-resolved mountain ranges may also introduce some errors, though they are smaller than the errors caused by lack of resolution of the flow itself. Therefore, simple centred finite difference representations of the equations written in flux form model discontinuities very well in general; though some caution may still be necessary when applying these schemes in meso-scale models.

APPENDIX

THE USE OF GLIMM'S METHOD TO SOLVE EQUATIONS (3) AND (5)

Glimm's method depends on being able to solve the Riemann problem exactly. Chorin (1976) modified an iterative method due largely to Godunov (1959) for this purpose, in order to solve the system of equations for gas dynamics utilising GM. Here we have followed the procedure adopted in MM, where use was made of the analogy between the shallow water equations (3) and (5) and the equations describing the isentropic flow of a perfect gas with constant specific heat (ie with $\gamma = 2$).

To make use of this analogy, let

$$\rho = \rho_w h \qquad (A1)$$

where ρ_w is the density of water and ρ is the analogous 'gas' density; and define the integrated pressure, using the hydrostatic assumption, by

$$P = \int_h^0 p\,dz = \int_h^0 -g\rho_w z\,dz ,$$

or

$$P = A\rho^\gamma \qquad (A2)$$

where $A = g/2\rho_w$ and $\gamma = 2$. Then equations (3) and (5) can be written as

$$\frac{\partial \underset{\sim}{u}}{\partial t} + \frac{\partial}{\partial x}\underset{\sim}{F}(\underset{\sim}{u}) = 0 \qquad (A3) ,$$

where $\underset{\sim}{u} = \begin{pmatrix} m \\ \rho \end{pmatrix}$, $\underset{\sim}{F} = \begin{pmatrix} m^2/\rho + A\rho^2 \\ m \end{pmatrix}$ and $m = \rho u$; or, equivalently,

$$\frac{\partial \underset{\sim}{u}}{\partial t} + B(\underset{\sim}{u})\frac{\partial \underset{\sim}{u}}{\partial x} = 0 \qquad (A3') ,$$

where $$B(\underset{\sim}{u}) = \begin{pmatrix} 2m/\rho & 2A\rho - (m/\rho)^2 \\ 1 & 0 \end{pmatrix} .$$

This enables one to obtain the slopes dx/dt of the two families of characteristic lines, $C_\pm$, which are given by the eigenvalues of B ,

$\lambda_{\pm} = u \pm c$, where $c = (\partial p / \partial \rho)^{1/2}$ is the sound speed.

Following MM equations (3) and (5) can be changed to

$$\left\{ \frac{\partial}{\partial t} + (u + \bar{c}) \frac{\partial}{\partial x} \right\} J_{+} = 0$$

$$\left\{ \frac{\partial}{\partial t} + (u - \bar{c}) \frac{\partial}{\partial x} \right\} J_{-} = 0 \quad ,$$

where $\bar{c} = (g h)^{1/2}$ (analogous to the sound speed in gas dynamics) is the speed of propagation of small disturbances relative to the fluid velocity, and $J_{\pm} = u \pm 2 \bar{c}$. The $J_{\pm}$ are called Riemann Invariants and are constant along the characteristic lines $C_{\pm}$. When characteristics of the same family intersect a discontinuity is formed, which moves with a speed s given by the jump conditions ($s [\underset{\sim}{u}] = [\underset{\sim}{F}(\underset{\sim}{u})]$, where $[\ldots]$ indicates the change in a quantity across the discontinuity) and the Riemann Invariants are no longer of any use. The jump conditions (and the full Rankine-Hugoniot conditions for non-isentropic flow) are obtained from the integral forms of the equations, Chorin and Marsden (1979).

Returning to the solution of the Riemann problem, consider equation (A3) with the initial data

$$\begin{aligned} u(x,0) &= S_{\ell} \equiv (\rho_{\ell}, u_{\ell}) , \quad x < 0 , \\ &= S_{r} \equiv (\rho_{r}, u_{r}) , \quad x \geq 0 . \end{aligned}$$

The S_{ℓ} and S_{r} indicate left and right initial states, respectively, separated by a slip-line with $dx/dt = u_{*}$. The solution at later times will consist of three states: S_{ℓ} , S_{r} and a centre state $S_{*} = (\rho_{*}, u_{*})$, separated by two (centred) waves (since there are two eigenvectors for matrix $\underset{\sim}{B}(\underset{\sim}{u})$), which may be either shocks or rarefaction waves. In our shallow water analogy, the shocks are replaced by hydraulic jumps and the rarefaction fans by depression waves, so that the profiles of water height are the same as the density profiles of Fig. A1. Figure A1 shows one of the four possible combinations of waves, with a shock wave travelling to the right (positive x-direction) and a rarefaction wave moving to the left. The three other possible combinations of waves

(dependent on the initial conditions) are either two (compressive) shock waves, two rarefaction waves, or the situation opposite to Fig. A1 with the shock moving to the left and the rarefaction to the right. Other possibilities, for instance connecting S_l to S_* (in Fig. A1) with a rarefaction shock whose speed satisfied the jump conditions, are forbidden by the entropy condition and do not exist in nature. The entropy condition is needed to pick out the physically relevant solution, because weak solutions of conservation laws are not uniquely determined by their initial values. It requires that the fluid crossing a shock suffer an increase in entropy. Its shallow water analogy is the energy condition, which requires that fluid crossing a jump suffer a loss of energy, ie particles only move across a jump from a region of lower total depth to a region of higher total depth.

We now return to the Chorin-Godunov iterative procedure for equation (A3) together with equation (A2). To solve the Riemann problem one needs to evaluate u_* and P_* (or ρ_*) in the centre state S_*. Let us define the quantity

$$M_l = (P_l - P_*)/(u_l - u_*) \qquad (A4).$$

If the left wave is a shock, it can be shown using the jump condition $s_l[\rho] = [\rho u]$, that

$$M_l = \rho_l (u_l - s_l) = \rho_* (u_* - s_l) \qquad (A5).$$

Similarly, let us define

$$M_r = (P_r - P_*)/(u_r - u_*) \qquad (A6).$$

If the right wave is a shock, one obtains

$$M_r = -\rho_r (u_r - s_r) = -\rho_* (u_* - s_r) \qquad (A7).$$

For either of the two cases (A4) or (A5) for M_l, and (A6) or (A7) for M_r, one can obtain

$$M_l = (\rho_l P_l)^{1/2} F(P_*/P_l) \qquad (A8),$$

$$M_r = (\rho_r P_r)^{1/2} F(P_*/P_r) \qquad (A9),$$

where

$$\begin{aligned} F(X) &= (X + X^{1/2})^{1/2}, \quad X \geq 1 \\ &= (1-X)/2\sqrt{2}\,(1-X^{1/4}), \quad X \leq 1 \end{aligned} \qquad (A10).$$

Upon elimination of u_* from (A4) and (A6), one obtains

$$P_* = (u_l - u_r + P_l/M_l + P_r/M_r)/(1/M_l + 1/M_r) \qquad \text{(A11)}.$$

The three equations (A8), (A9) and (A11) have three unknowns, which can be found using an iterative procedure. We followed the procedure detailed by Chorin (1976), which included a modification to deal with occasional failure of the iteration to converge for strong rarefactions. The iteration was started by choosing an initial value for P_* that was the mean value of P_l and P_r, and then calculating the initial values of M_l and M_r from (A8) and (A9) respectively.

After P_*, M_l and M_r have been determined, one can obtain u_* by eliminating P_* from the definitions of M_l and M_r, to give

$$u_* = (P_l - P_r + M_l u_l + M_r u_r)/(M_l + M_r) .$$

The complete solution to this Riemann problem can be obtained using the jump conditions for shock waves and (since the flow is adiabatic in smooth regions) the isentropic law and constancy of the Riemann Invariants for the rarefaction waves. This solution is then sampled.

For the computer implementation of GM, there are four main cases. If the sample point P_i lies to the right of the slip-line (ie $\theta \Delta x > u_* \Delta t/2$) there are two cases:

1. If $P_* > P_r$, the right wave is a shock.

   a. If P_i lies to the left of the shock line defined by $dx/dt = s_r$, one has $u = u_*$ and $\rho = \rho_*$;

   b. If P_i lies to the right of the shock line, one has $u = u_r$ and $\rho = \rho_r$.

2. If $P_* \leqslant P_r$, the right wave is a rarefaction wave. This is bounded on the left by the line defined by $dx/dt = u_* + c_*$, where $c_* = (\gamma P_*/\rho_*)^{1/2}$, and on the right by the line defined by $dx/dt = u_r + c_r$, where $c_r = (\gamma P_r/\rho_r)^{1/2}$.

   a. If P_i lies to the left of the rarefaction wave, then $u = u_*$ and $\rho = \rho_*$;

   b. If P_i lies to the right of it, then $u = u_r$ and $\rho = \rho_r$;

   c. If P_i lies inside the right rarefaction wave, one equates the slope of the C_+ characteristic, $dx/dt = u + c$, to the slope of the line through the origin and ($\theta \Delta x$, $\Delta t/2$), obtaining

$$u + c = 2\theta \Delta x / \Delta t \qquad \text{(A12)}.$$

From the constancy of the J_- Riemann Invariant along the C_- characteristics (which cross the rarefaction)

$$c = c_r + \tfrac{1}{2}(u - u_r) \qquad \text{(A13)},$$

and substituting into (A12) one obtains

$$u = \tfrac{1}{3}(u_r - 2c_r + 4\theta \Delta x/\Delta t) \qquad \text{(A14)}.$$

By substituting (A14) back into (A13) one can obtain c, which is then used to evaluate ρ, using $c = (\gamma P/\rho)^{1/2}$ and (A2).

The other two cases, with P_i lying to the left of the slip-line, and the left wave being either a shock or a rarefaction wave, are mirror images of cases 1 and 2, with C_+, J_- replaced by C_-, J_+, and will not be described in detail (see Sod 1978 for full details and a flow diagram).

References

Chorin, A J 1976 Random choice solution of hyperbolic systems, J. Comp. Phys., 22, 517-533.

Chorin, A J and Marsden, J E 1979 A mathematical introduction to fluid mechanics, Springer-Verlag, New York/ Berlin.

Colella, P 1982 Glimms method for gas dynamics, SIAM J. Sci. Stat. Comp., 3, 76-110.

Francis, P E 1975 The use of a multipoint filter as a dissipative mechanism in a numerical model of the general circulation of the atmosphere, Quart. J. R. Met. Soc., 101, 567-582.

Glimm, J 1965 Solutions in the large for non-linear hyperbolic systems of equations, Comm. Pure Appl. Math., 18, 697-715.

Godunov, S K 1959 A finite difference method for the numerical computation of discontinuous solutions of the equations of fluid dynamics, Mat. Sbornik, 47, 271-306.

Houghton, D D and Kasahara, A A 1968 Nonlinear shallow fluid flow over an isolated ridge, Comm. Pure Appl. Math., 21, 1-23.

Lax, P D	1973	Hyperbolic systems of conservation laws and the mathematical theory of shock waves, SIAM Regional Conf. Series in Appl. Math., No. 11, 1-48.
Marshall, G and Mendez, R	1981	Computational aspects of the random choice method for shallow water equations, J. Comp. Phys., 39, 1-21.
Marshall, G and Menendez, A N	1981	Numerical treatment of nonconservation forms of the equations of shallow water theory, J. Comp. Phys., 44, 167-188.
Shapiro, R	1971	The use of linear filtering as a parameterization of atmospheric diffusion, J. Atmos. Sci., 28, 523-531.
Sod, G A	1978	A survey of several finite difference methods for systems of nonlinear hyperbolic conservation laws, J. Comp. Phys., 27, 1-31.
Tepper, M	1950	A proposed mechanism of squall lines: the pressure jump line, J. Met. 7, 21-29.
Wallace, J M, Tibaldi, S and Simmons, A J	1982	A study of the relationship between the orography and systematic errors of the ECMWF model, GARP WRCP NEP rep. no. 3 (I D Rutherford ed), 5.1-5.5.
Williams, R T and Hori, A M	1970	Formation of hydraulic jumps in a rotating system, J Geophys. Res., 75, 2813-2821.

List of Figures

Figure 1. The sampling procedure for v.

Figures 2-6. Results from the first experiment described in (a), using GM with $p_1 = 5$, $p_2 = 3$ and $N = 320$, consisting of a sequence of profiles of u', v' and h' showing the formation and evolution of the hydraulic jump up to $t = 2.8\, L/U$.

Figure 7. The FDM result equivalent to Fig. 6, with $K = 2.5 \times 10^{4}\, m^2 s^{-1}$ and $N = 320$. Superimposed is the h profile from a similar run with the finite difference model that used a non-conservative formulation of the equations (dashed line).

Figures 8 and 9 Results from a repeat run of the FDM experiment (a) using a 17-point filter instead of artificial diffusion, for $t = 1.05\, L/U$ (Fig. 8) and $t = 2.8\, L/U$ (Fig. 9).

Figure 10 Results at $t = 1.4\, s$ for a repeat of HK's experiment using the FDM with $K = 2 \times 10^{-3}\, m^2 s^{-1}$ and N = 2000.

Figure 11 As Fig. 10, but for GM with $p_1 = 3$, $p_2 = 2$.

Figure 12 Results at $t = 2.1\, s$ for the ridge + rotation experiment $(R_o = 1.0)$, using the FDM with $K = 2 \times 10^{-3}\, m^2 s^{-1}$ and N = 2000.

Figure 13 As Fig. 12, but for GM with $p_1 = 2$, $p_2 = 1$.

Figure 14 — Results at $t = 2.4s$ for the experiment described in section (iii), with N = 2000. The profiles from GM (with $\rho_1 = 2$, $\rho_2 = 1$) are shown in full, and the profiles from the FDM have been added (the dashed lines) where they differ from GM's.

Figure 15 — Results from the FDM (N = 50) for flow over the double ridge with (I), the mean height of topography representation. The profiles of h and H for N = 2000 have been added (the dashed lines).

Figure 16 — As Fig. 15, but with (II), the maximum height of topography representation.

Figure A1 — Solution of a Riemann problem with $\rho_l > \rho_r$: a shock-wave moving to the right and a rarefaction-wave moving to the left.

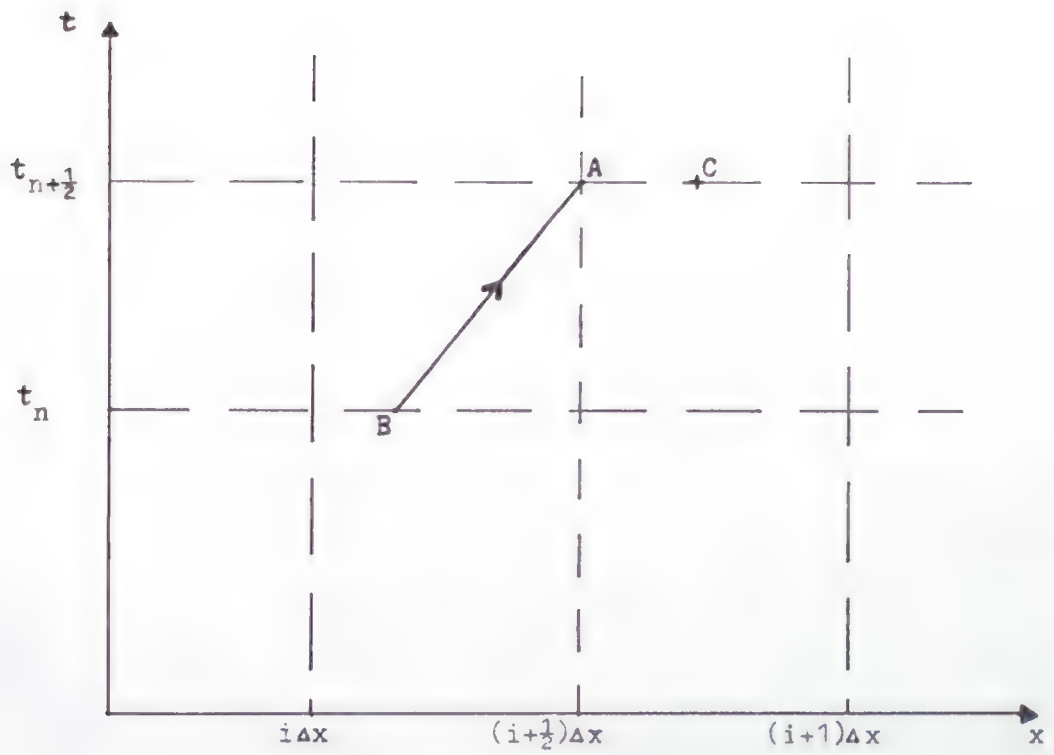

Figure 1.

A = fixed sampling point for v, at time $t_{n+\frac{1}{2}}$.

B = point $\mathbf{P}_i^n$, from which the value of v is taken forward to $t_{n+\frac{1}{2}}$.

C = random sampling point for u and ρ, P_i.

Slope of AB = $u^{n+\frac{1}{2}}((i+\frac{1}{2})\Delta x)^{-1}$.

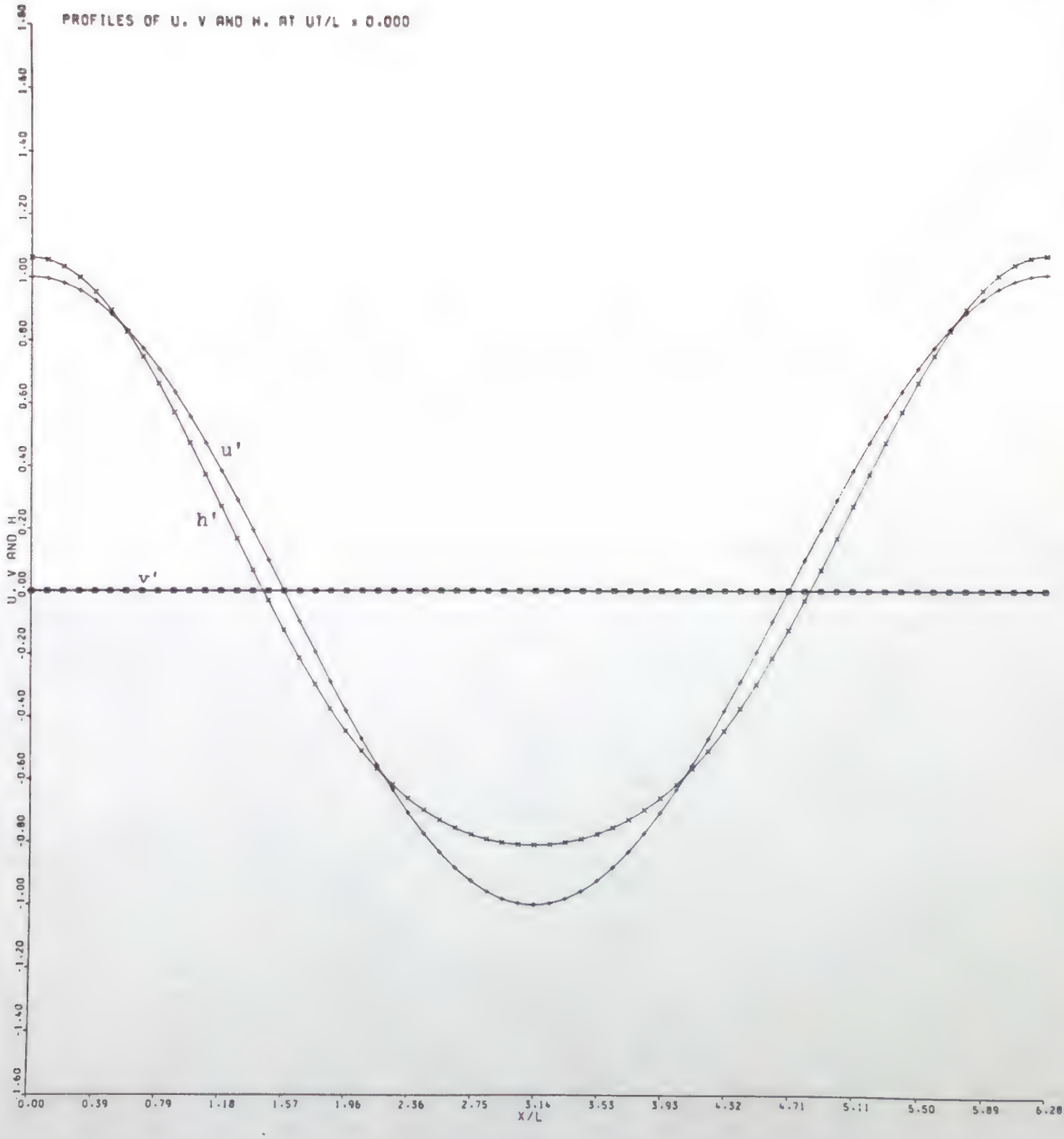
PROFILES OF U, V AND H, AT UT/L = 0.000
U, V AND H
X/L
u'
h'
v'
1.60
1.40
1.20
1.00
0.80
0.60
0.40
0.20
0.00
-0.20
-0.40
-0.60
-0.80
-1.00
-1.20
-1.40
-1.60
0.00
0.39
0.79
1.18
1.57
1.96
2.36
2.75
3.14
3.53
3.93
4.32
4.71
5.11
5.50
5.89
6.28

Figure 2

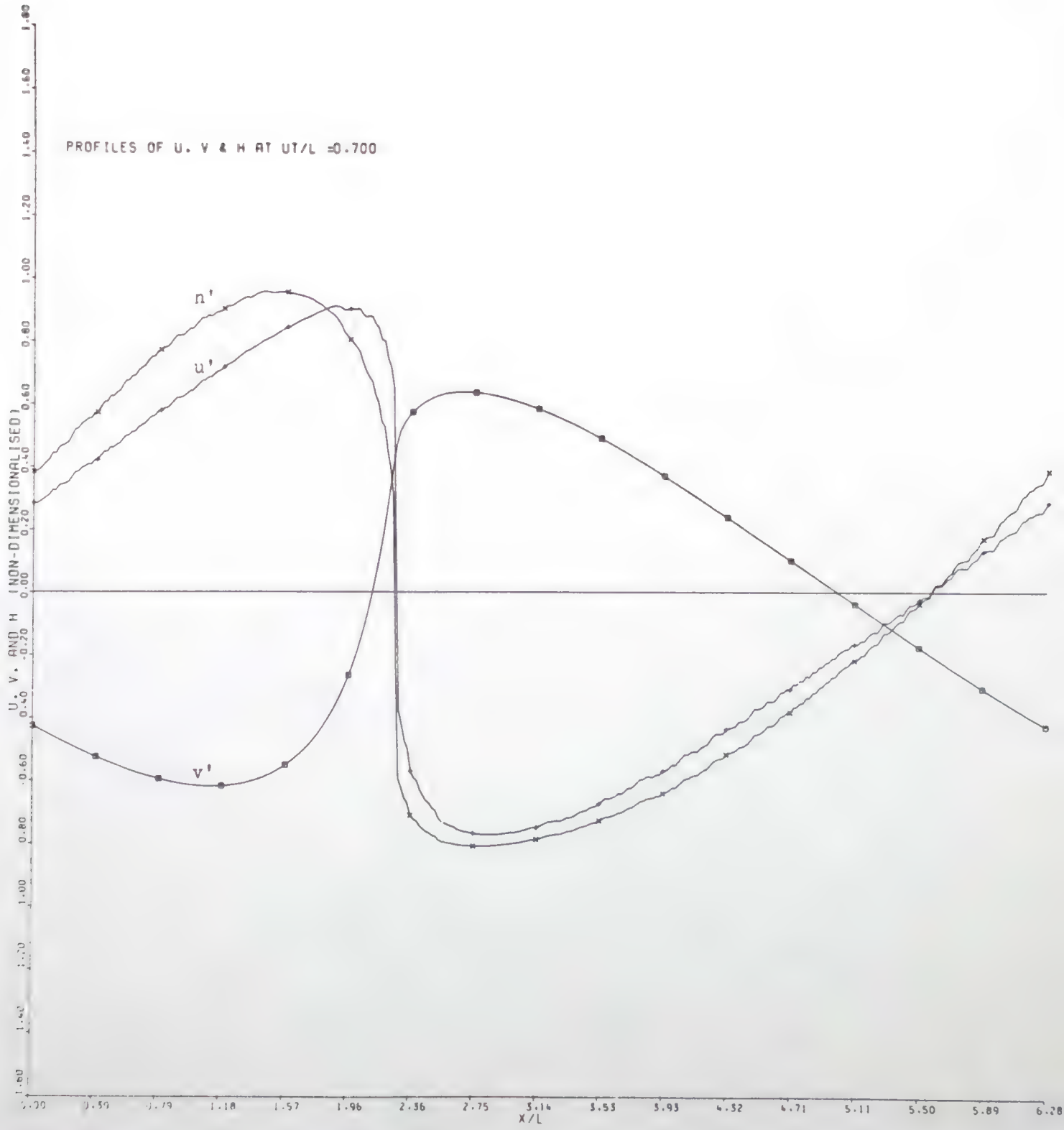
PROFILES OF U. V & H AT UT/L =0.700
n'
u'
v'
U, V, AND H (NON-DIMENSIONALISED)
X/L
1.60
1.40
1.20
1.00
0.80
0.60
0.40
0.20
0.00
-0.20
-0.40
-0.60
-0.80
-1.00
-1.20
-1.40
-1.60
0.00
0.39
0.79
1.18
1.57
1.96
2.36
2.75
3.14
3.53
3.93
4.32
4.71
5.11
5.50
5.89
6.28

Figure 3

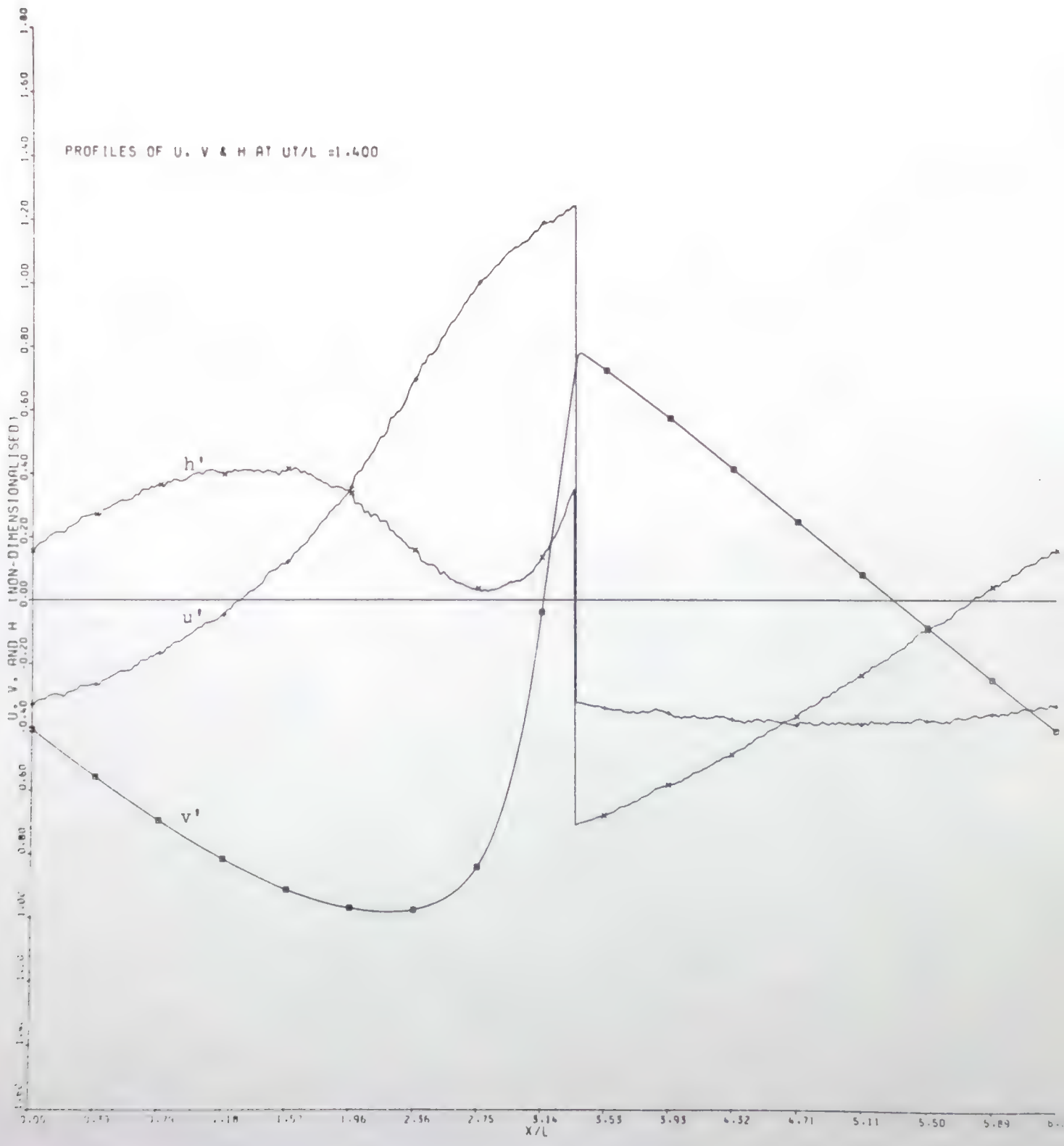
PROFILES OF U, V & H AT UT/L =1.400
U, V, AND H (NON-DIMENSIONALISED)
h'
u'
v'
X/L

Figure 4

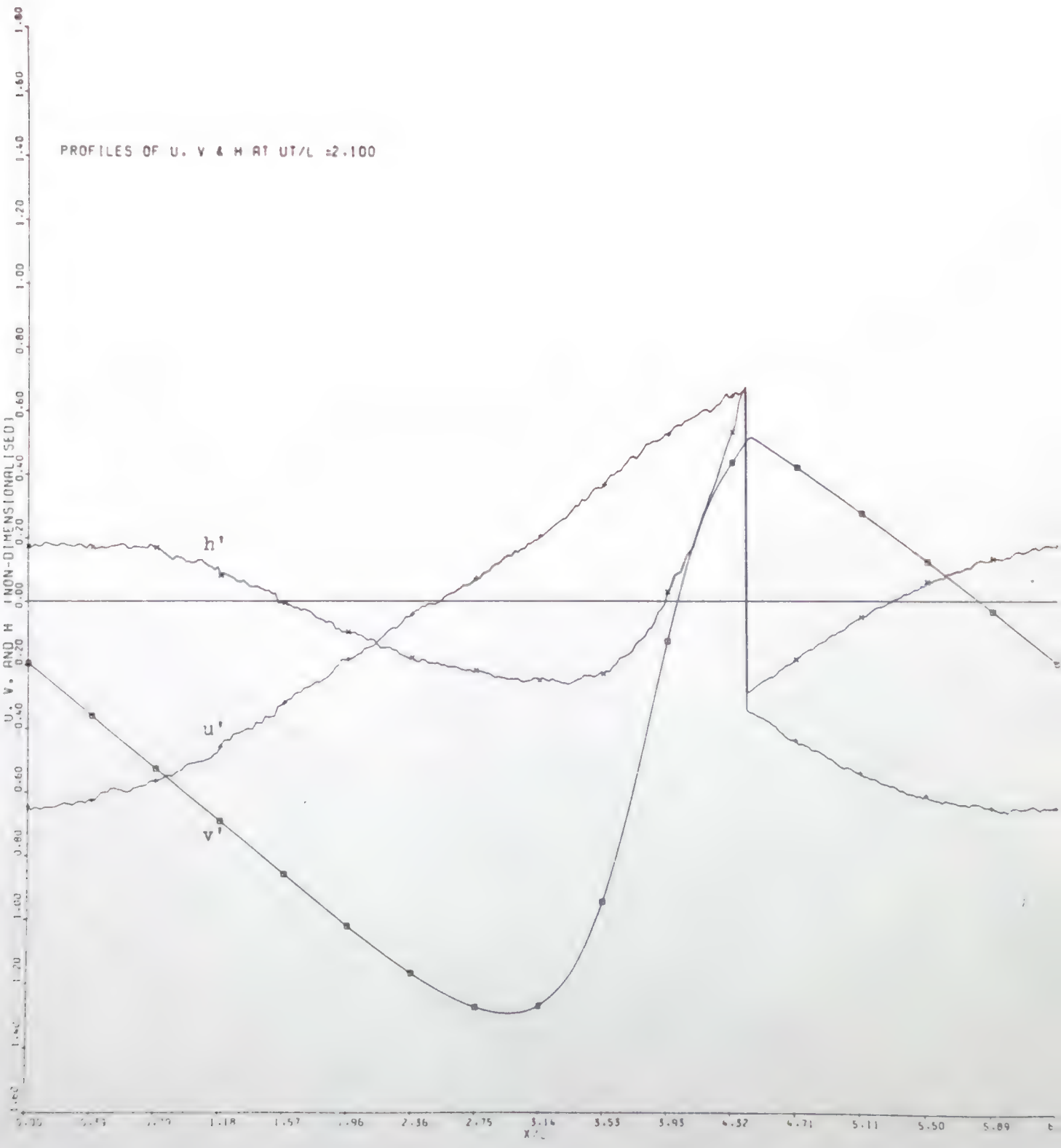
PROFILES OF U, V & H AT UT/L =2.100
U, V, AND H (NON-DIMENSIONALISED)
h'
u'
v'
1.60
1.40
1.20
1.00
0.80
0.60
0.40
0.20
0.00
0.20
0.40
0.60
0.80
1.00
1.18
1.57
1.96
2.36
2.75
3.14
3.53
3.93
4.32
4.71
5.11
5.50
5.89

Figure 5

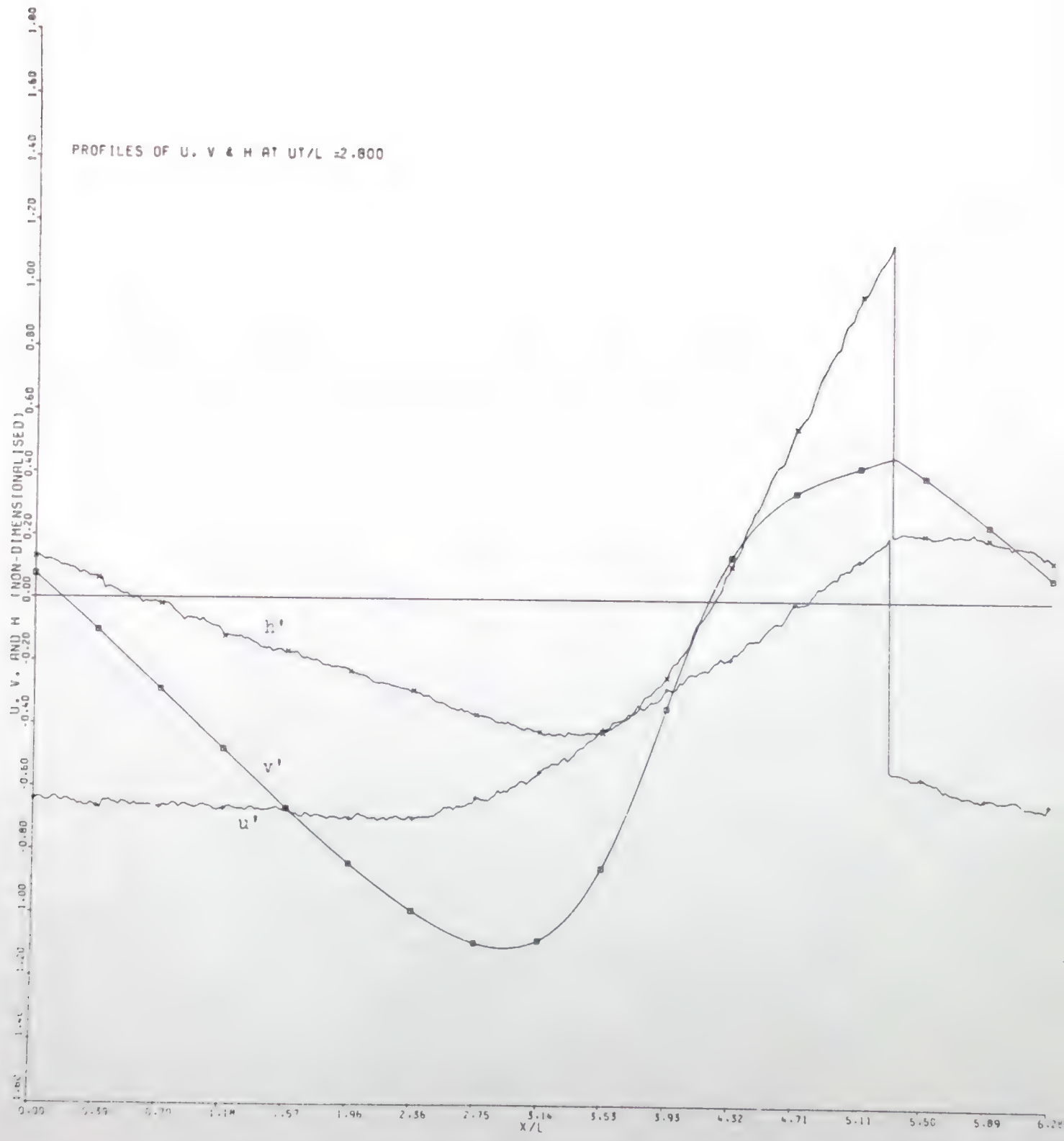
PROFILES OF U, V & H AT UT/L =2.800
U, V, AND H (NON-DIMENSIONALISED)
1.60
1.40
1.20
1.00
0.80
0.60
0.40
0.20
0.00
-0.20
-0.40
-0.60
-0.80
-1.00
h'
v'
u'
0.00
2.36
2.75
3.14
3.53
3.93
4.32
4.71
5.11
5.50
5.89
X/L

Figure 6

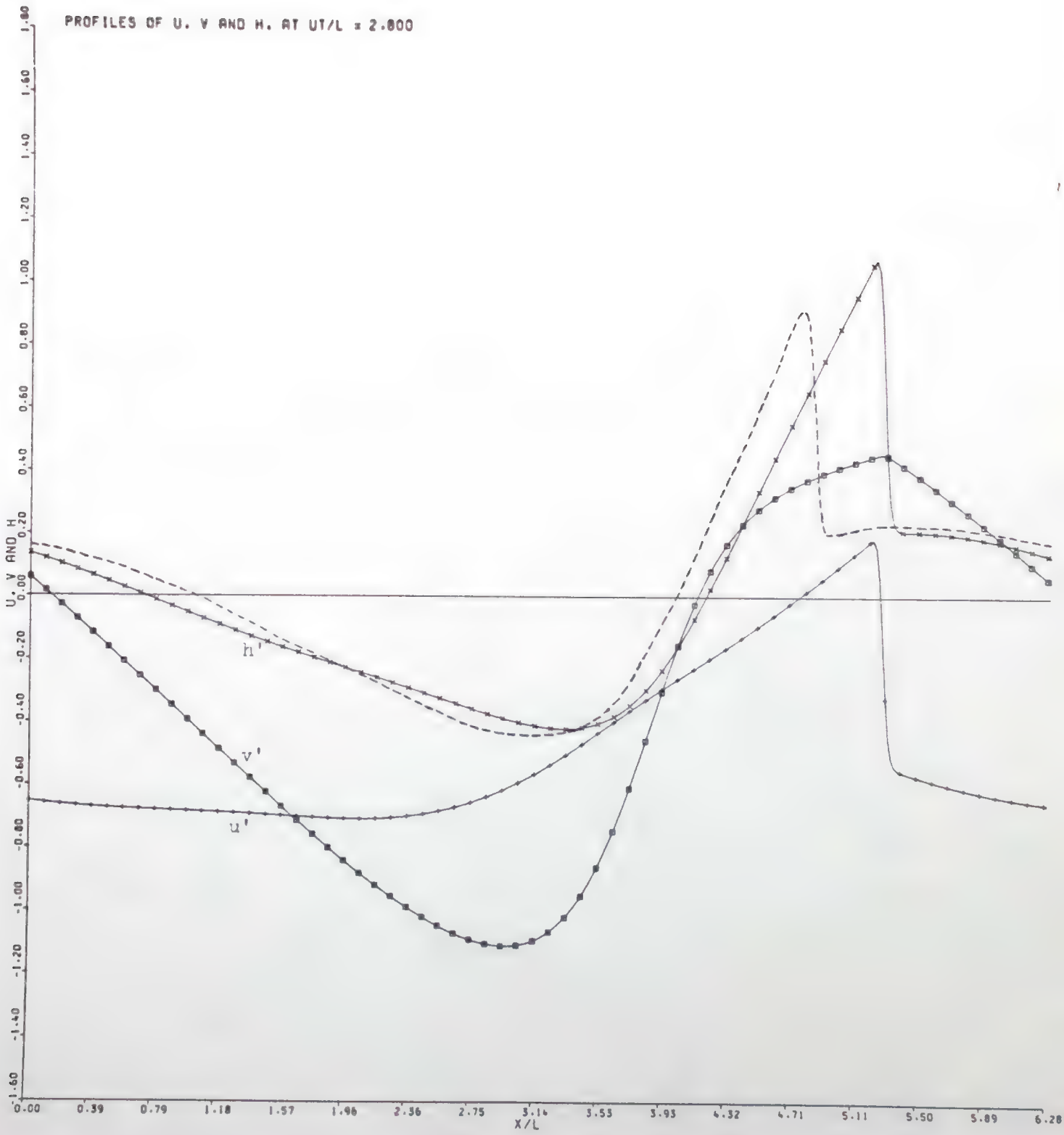
PROFILES OF U, V AND H, AT UT/L = 2.800
U', V AND H
X/L
h'
v'
u'
1.80
1.60
1.40
1.20
1.00
0.80
0.60
0.40
0.20
0.00
-0.20
-0.40
-0.60
-0.80
-1.00
-1.20
-1.40
-1.60
0.00
0.39
0.79
1.18
1.57
1.96
2.36
2.75
3.14
3.53
3.93
4.32
4.71
5.11
5.50
5.89
6.28

Figure 7

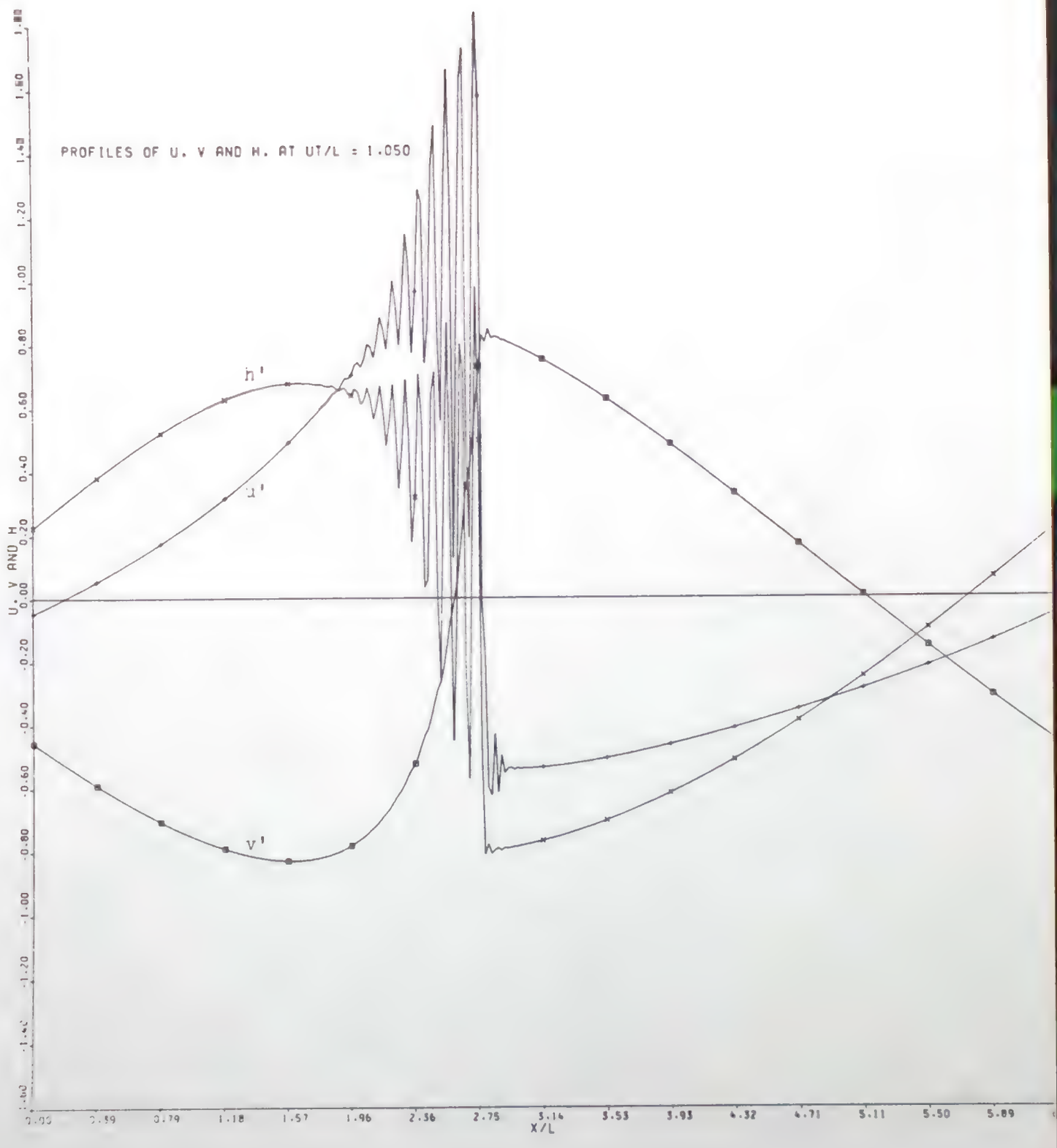

Figure 8

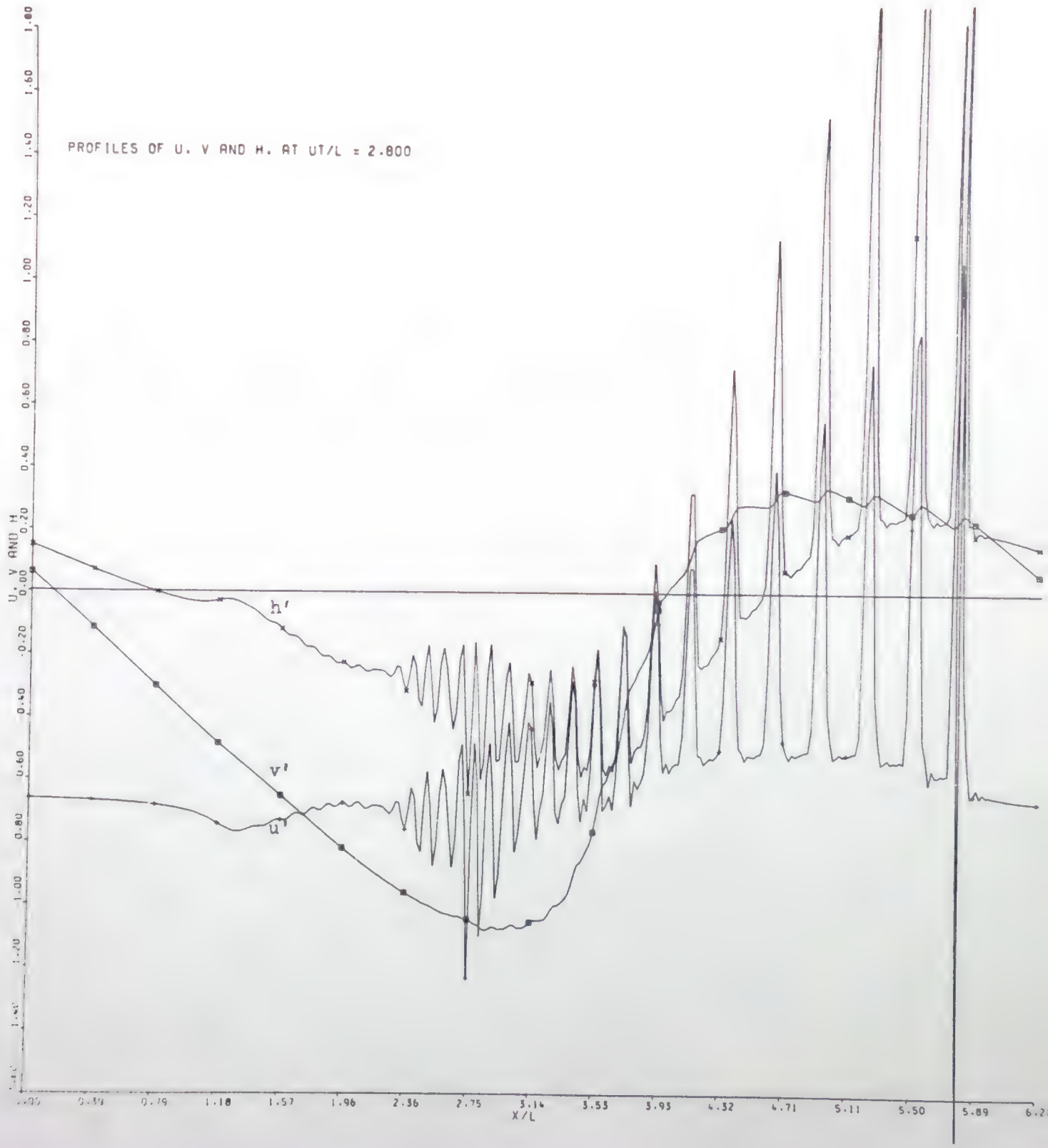

Figure 9

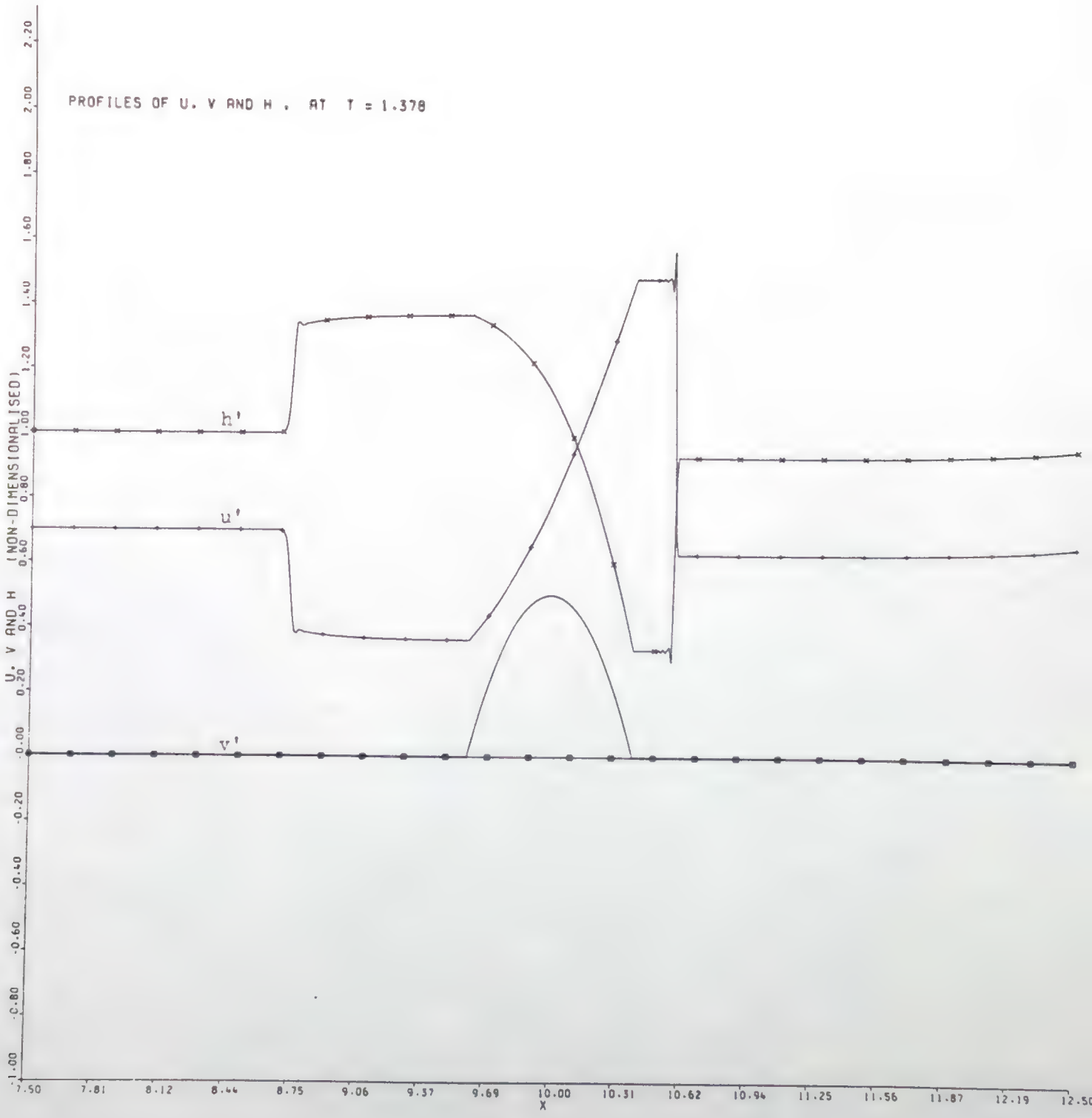
PROFILES OF U. V AND H . AT T = 1.378
U. V AND H (NON-DIMENSIONALISED)
2.20
2.00
1.80
1.60
1.40
1.20
1.00
0.80
0.60
0.40
0.20
0.00
-0.20
-0.40
-0.60
-0.80
-1.00
h'
u'
v'
7.50
7.81
8.12
8.44
8.75
9.06
9.37
9.69
10.00
10.31
10.62
10.94
11.25
11.56
11.87
12.19
12.50
X

Figure 10

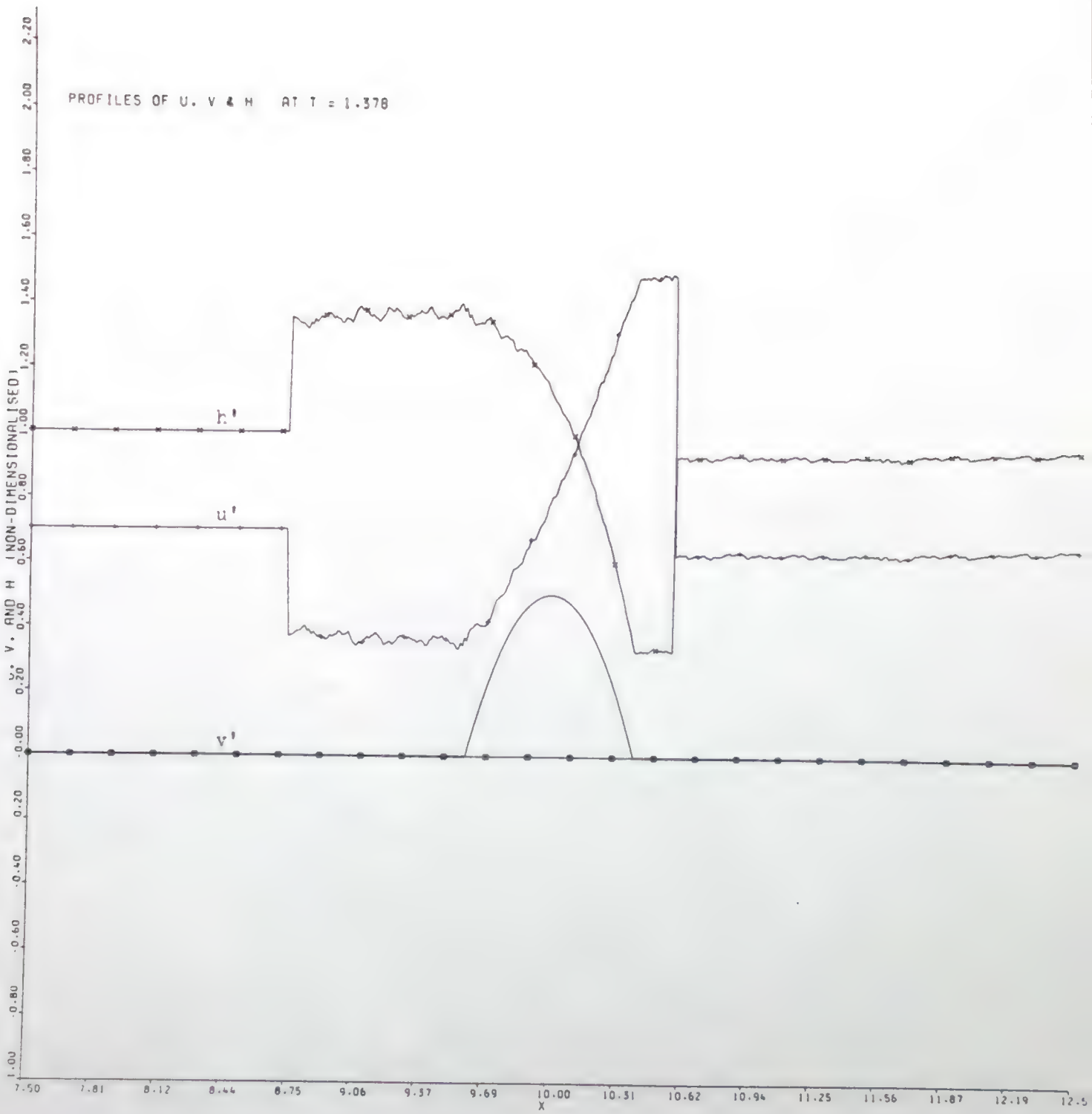
PROFILES OF U. V & H AT T = 1.378
U, V, AND H (NON-DIMENSIONALISED)
h'
u'
v'
2.20
2.00
1.80
1.60
1.40
1.20
1.00
0.80
0.60
0.40
0.20
0.00
-0.20
-0.40
-0.60
-0.80
-1.00
7.50
7.81
8.12
8.44
8.75
9.06
9.37
9.69
10.00
10.31
10.62
10.94
11.25
11.56
11.87
12.19
12.5
X

Figure 11

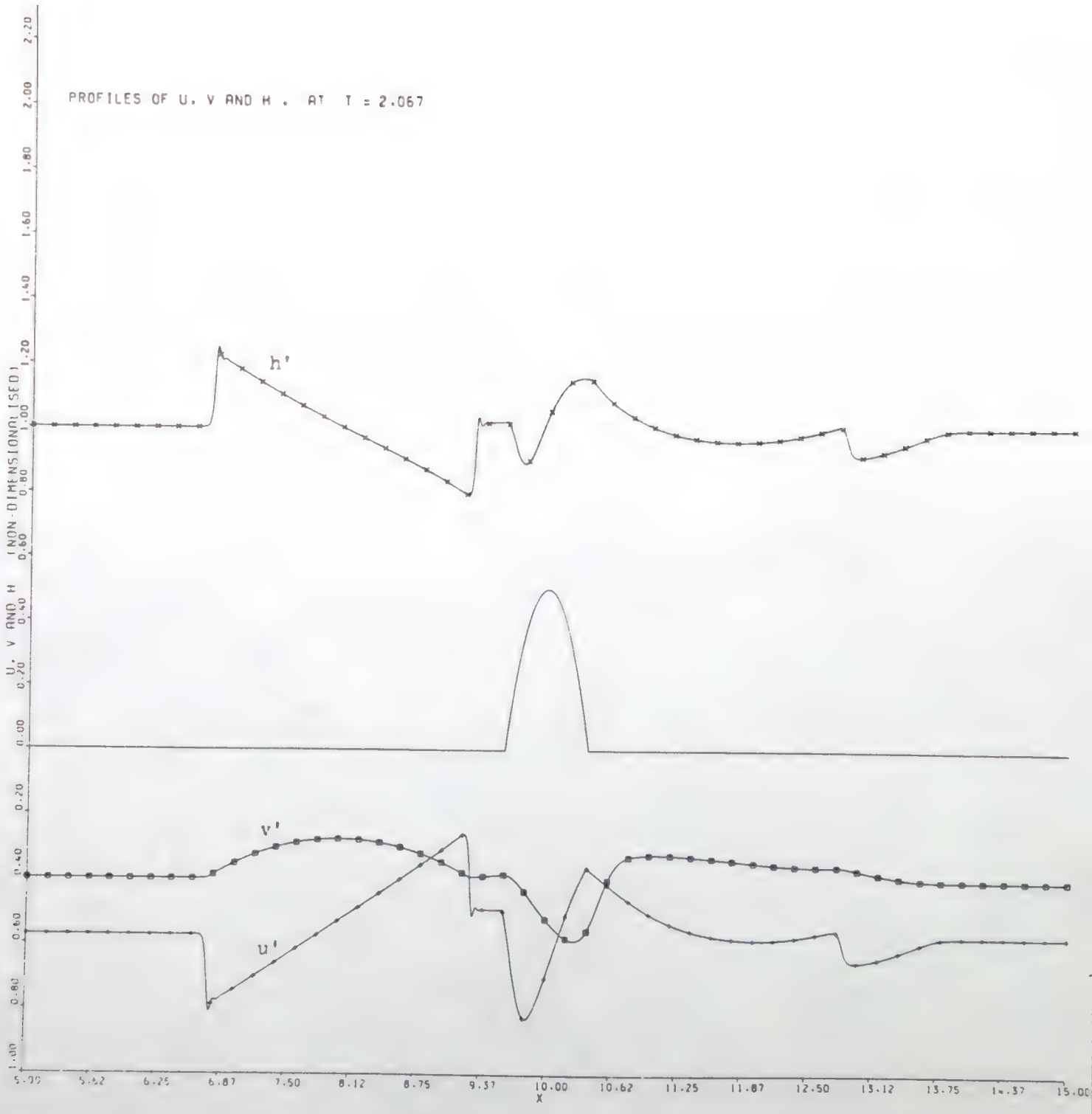
PROFILES OF U, V AND H , AT T = 2.067
U, V AND H (NON-DIMENSIONALISED)
h'
v'
u'
X

Figure 12

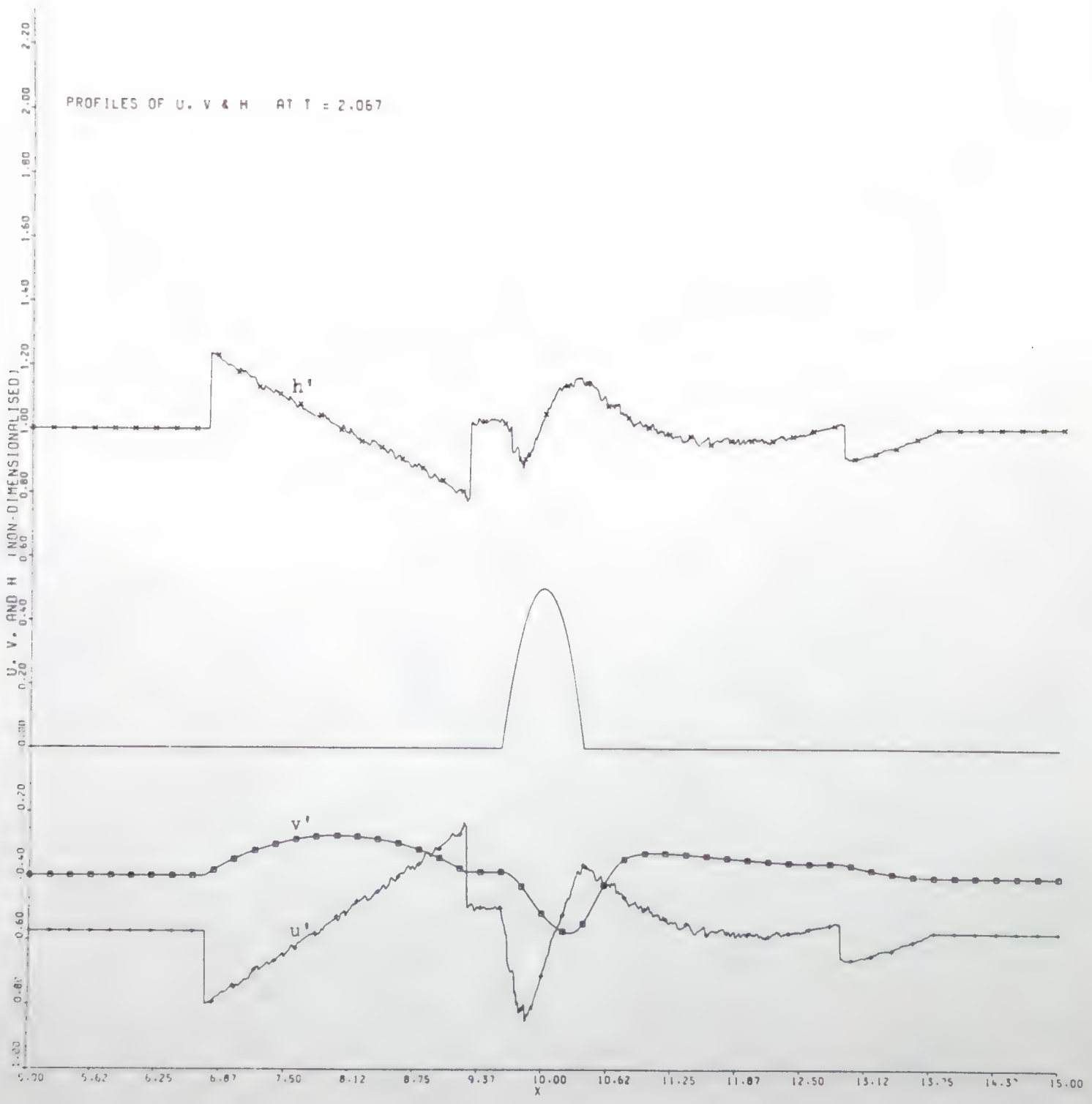
PROFILES OF U. V & H AT T = 2.067
U. V. AND H (NON-DIMENSIONALISED)
h'
v'
u'
X
5.00
5.62
6.25
6.87
7.50
8.12
8.75
9.37
10.00
10.62
11.25
11.87
12.50
13.12
13.75
15.00

Figure 13

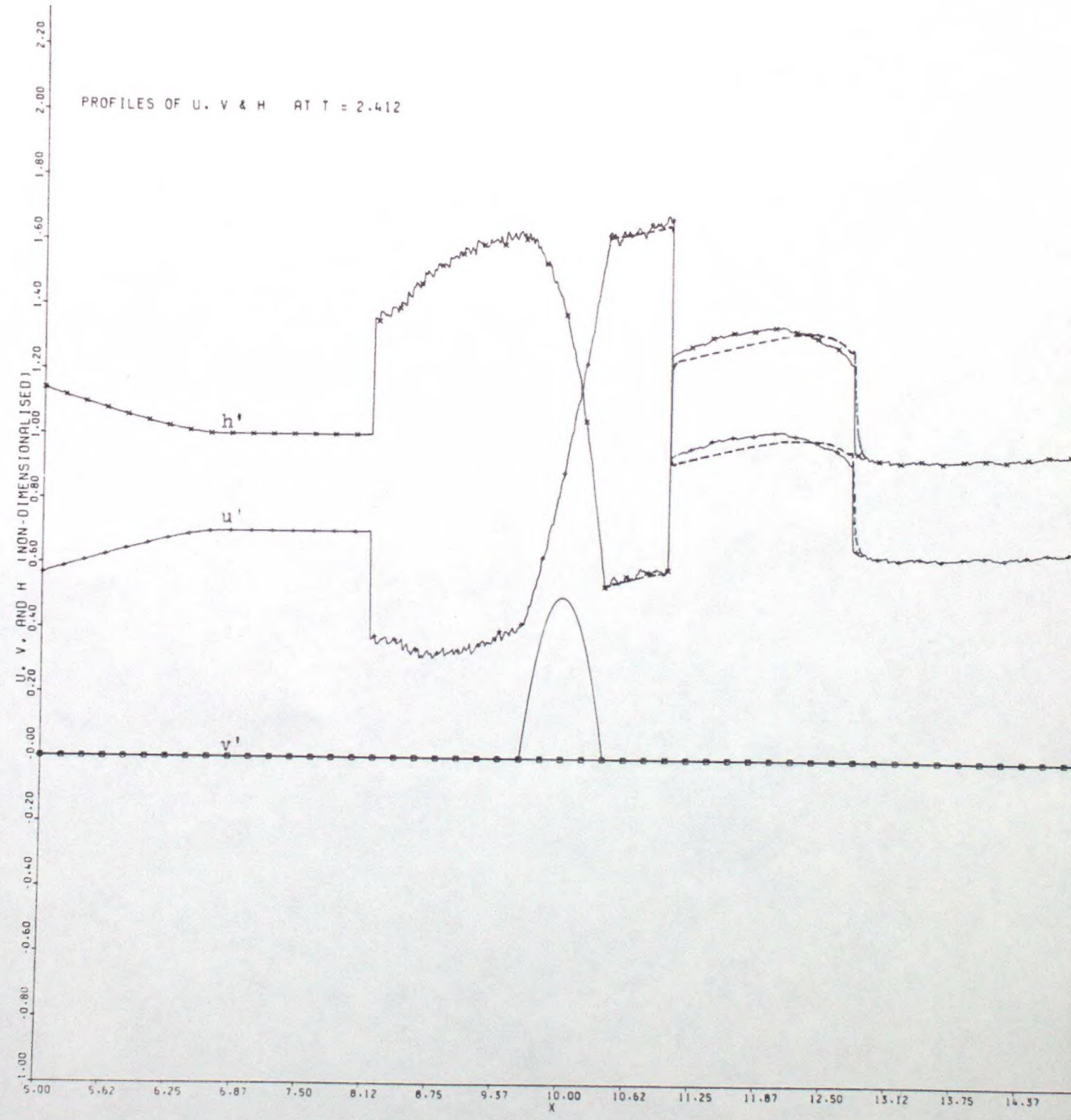
PROFILES OF U. V & H AT T = 2.412
U. V. AND H (NON-DIMENSIONALISED)
2.20
2.00
1.80
1.60
1.40
1.20
1.00
0.80
0.60
0.40
0.20
-0.00
-0.20
-0.40
-0.60
-0.80
-1.00
h'
u'
v'
5.00
5.62
6.25
6.87
7.50
8.12
8.75
9.37
10.00
10.62
11.25
11.87
12.50
13.12
13.75
14.37
X

Figure 14

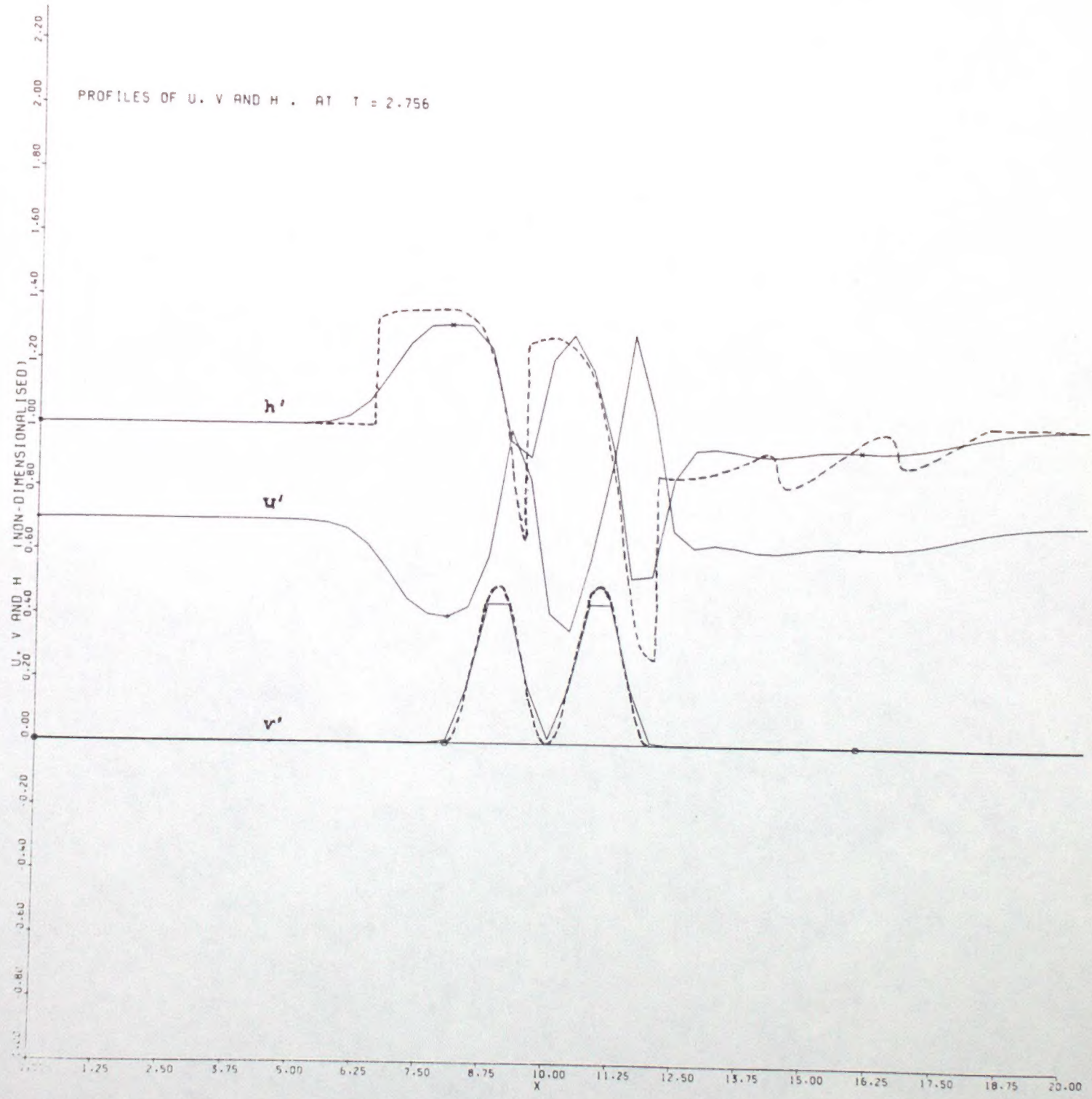
PROFILES OF U. V AND H . AT T = 2.756
U. V AND H (NON-DIMENSIONALISED)
h'
u'
v'
X
2.20
2.00
1.80
1.60
1.40
1.20
1.00
0.80
0.60
0.40
0.20
0.00
-0.20
-0.40
-0.60
1.25
2.50
3.75
5.00
6.25
7.50
8.75
10.00
11.25
12.50
13.75
15.00
16.25
17.50
18.75
20.00

Figure 15

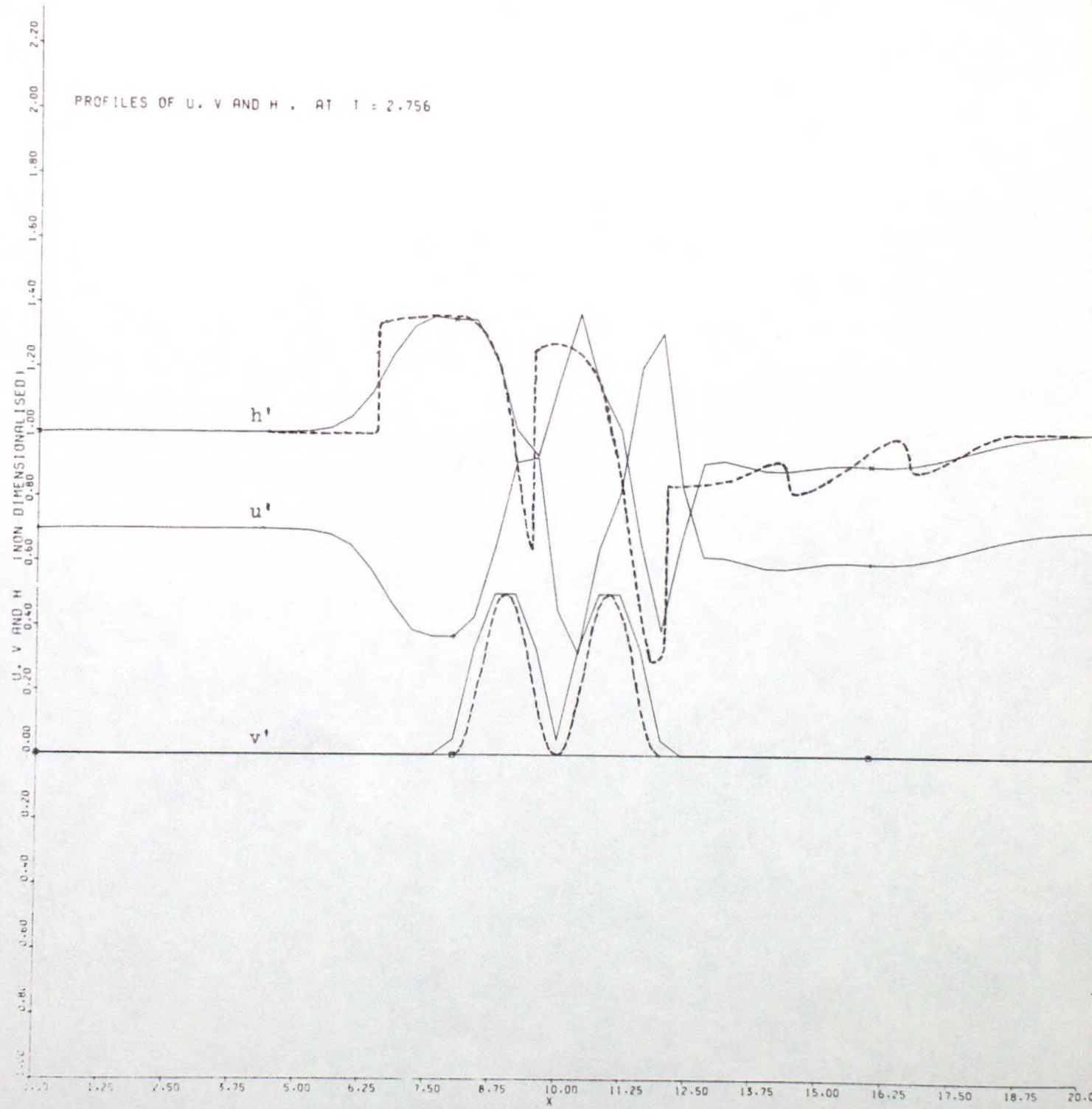
PROFILES OF U. V AND H . AT T = 2.756
U, V AND H (NON DIMENSIONALISED)
h'
u'
v'
X

Figure 16

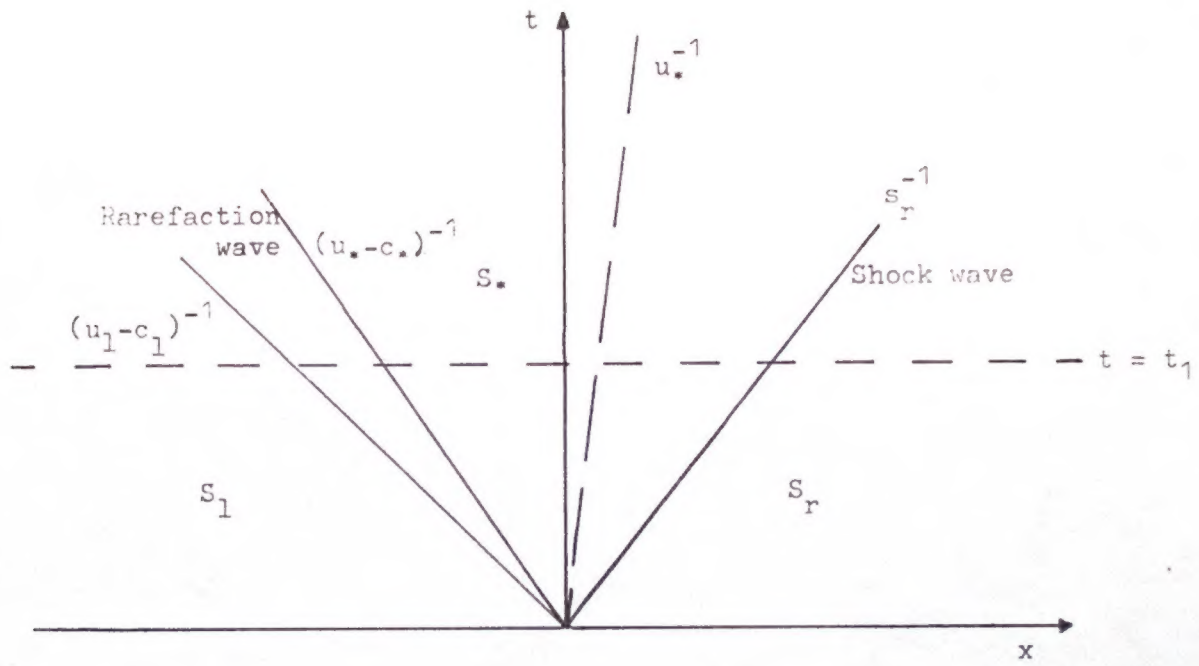
t
u_*^{-1}
s_r^{-1}
Rarefaction wave
$(u_*-c_*)^{-1}$
S_*
Shock wave
$(u_l-c_l)^{-1}$
$t = t_1$
S_l
S_r
x

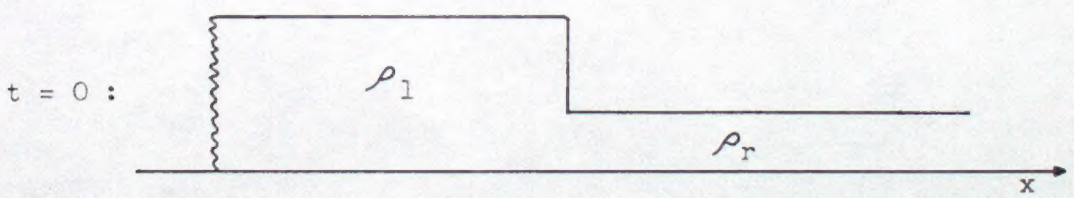
t = 0 :
ρ_l
ρ_r
x

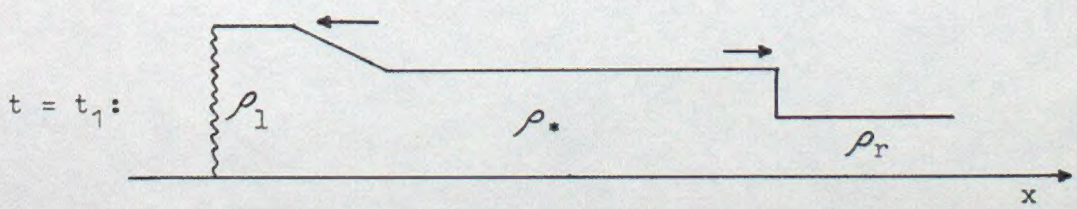
$t = t_1$:
ρ_l
ρ_*
ρ_r
x

Figure A1